Formation of Zn-Ca Phyllomanganate Nanoparticles in Grass Roots

Bruno Lanson[a], Matthew A. Marcus[b], Sirine Fakra[b], Frédéric Panfili[a], Nicolas Geoffroy[a], Alain Manceau[a]

[a] Mineralogy & Environments Group, Maison des GéoSciences, Université Joseph Fourier – CNRS, F-38041 Grenoble Cedex 9, France.

[b] Advanced Light Source, Lawrence Berkeley National Laboratory, Berkeley, California 94720, USA

* Corresponding author: Bruno.Lanson@obs.ujf-grenoble.fr

Running title: Zn-Ca Phyllomanganate Nanoparticles in Grass Roots

Abstract. It is now well established that a number of terrestrial and aquatic microorganisms have the capacity to oxidize and precipitate Mn as phyllomanganate. However, this biomineralization has never been shown to occur in plant tissues, nor has the structure of a natural Mn(IV) biooxide been characterized in detail. We show that the graminaceous plant *Festuca rubra* (red fescue) produces a Zn-rich phyllomanganate with constant Zn:Mn and Ca:Mn ratios (0.46 and 0.38, respectively) when grown on a contaminated sediment. This new phase is so far the Zn-richest manganate known to form in nature (chalcophanite has a Zn:Mn ratio of 0.33) and has no synthetic equivalent. Visual examination of root fragments under a microscope shows black precipitates about ten to several tens of microns in size, and their imaging with backscattered and secondary electrons demonstrates that they are located in the root epidermis. In situ measurements by Mn and Zn K-edge extended X-ray absorption fine structure (EXAFS) spectroscopy and X-ray diffraction (XRD) with a micro-focused beam can be quantitatively described by a single-phase model consisting of Mn(IV) octahedral layers with 22% vacant sites capped with tetrahedral and octahedral Zn in proportions of 3:1. The layer charge deficit is also partly balanced by interlayer Mn and Ca. Individual crystallites have a domain radius of 33 Å in the *ab* plane and contain only 1.2 layers (~8.6 Å) on average. Since this biogenic Mn oxide consists mostly of isolated layers, basal 00*l* reflections are essentially absent despite its lamellar structure. Individual Mn layers are probably held together in the Mn-Zn precipitates by stabilizing organic molecules. Zinc biomineralization by plants likely is a defense mechanism against toxicity induced by excess concentrations of this metal in the rhizosphere.

1. INTRODUCTION

Graminaceous plants, like other so-called metal-tolerant plants, mostly sequester metals in roots to protect reproductive and photosynthetic tissues (Li et al., 2000; Simon, 2005). The ability to store metals in underground tissues is used in phytoremediation to reinstall a vegetation cover on heavily contaminated areas and limit the propagation of metals into the food chain (Smith and Bradshaw, 1992; Cunningham et al., 1995; Vangronsveld et al., 1995; Ma et al., 2003; Mench et al., 2003; Krämer, 2005). Panfili et al. (2005) showed that the grass species *Festuca rubra* (red fescue) and *Agrostis tenuis* (colonial bentgrass) accelerate the weathering of zinc sulfide when grown on contaminated dredged sediment, thus increasing Zn bioavailability in the rhizosphere. After two years of plant growth, micrometer-sized Mn-Zn black precipitates were observed at the surface of *Festuca rubra* roots, but not characterized (Panfili, 2004). Zinc precipitation may be a bioactive tolerance mechanism in response to metal toxicity, or a passive mineralization at the soil-root interface (Cotter-Howells et al., 1999). Clarifying this issue and determining the mineralogy and structure of this natural precipitate is important to enhance the effectiveness of using graminaceous plants in phytoremediation. These questions are addressed here with electron microscopy and synchrotron-based microanalytical tools, including X-ray fluorescence (μ-XRF), extended X-ray absorption fine structure (μ-EXAFS) spectroscopy and X-ray diffraction (μ-XRD) (Manceau et al., 2002b). Micro-XRD was employed to determine the nanocrystalline structure of the Mn-Zn precipitates and the nature of defects (layer stacking faults, cationic vacancies and occupancies, Mn, Zn, and Ca site configuration, stoichiometry) through modeling of their scattering properties (Villalobos et al., 2006; Drits et al., 2007). We show that the root precipitates are present in the root epidermis (the outermost layer of root cells) and consist of a poorly crystallized phyllomanganate with a constant Zn:Mn ratio higher than reported so far

for any natural and synthetic manganate. A structure model is proposed for this new biomineral.

2. MATERIALS AND METHODS

2.1 Materials

The composition in major elements of the dredged sediment was 68.3 % SiO_2, 6.9 % CaO, 4.8 % Al_2O_3, 2.4 % Fe_2O_3, 0.7 % P_2O_5, and 7.2% organic carbon, and the composition in a trace metals was 4700 $mg.kg^{-1}$ Zn, 700 $mg.kg^{-1}$ Pb, and ~270 $mg.kg^{-1}$ Mn. Seeds of *F. rubra* were sown in plastic pots filled with 40 kg of either the untreated sediment, the sediment amended with 3 wt. % hydroxylapatite, or the sediment amended with 5 wt. % Thomas basic slag. The pots were placed in a greenhouse without artificial lighting and daily irrigated with tap water in an amount similar to the mean rainfall in northern France. After two years of culture, the pots were dismantled to collect samples. The texture and color of the sediment in areas colonized by the roots (upper 30 cm of the pots) were similar to a brown silty soil, whereas the initial sediment was black and compact. Roots of *F. rubra* from the treated and untreated pots were washed meticulously with distilled water to remove soil particles from the surface and then freeze-dried.

The speciation of zinc in the initial sediment and in the rhizosphere of *F. rubra* after the two years of vegetation was described previously (Panfili et al., 2005). Briefly, in the untreated and unvegetated sediment, Zn was distributed as ~50% (mol ratio of total Zn) sphalerite, ~40% Zn-ferrihydrite, and ~10 to 20% (Zn-Al)-hydrotalcite plus Zn-phyllosilicate. In the presence of plants, ZnS was almost completely dissolved, and the released Zn bound to phosphate (~40–60%) and to Zn phyllosilicate plus (Zn,Al)-hydrotalcite (~20–40%). The co-addition of mineral amendment did not affect the Zn speciation in the vegetated sediment.

2.2 Methods

2.2.1 Electron microscopy

Regions of the roots rich in black precipitates were carbon-coated and examined in secondary and backscattered electron modes by high-resolution scanning electron microscopy (JEOL JSM-6320F with a field emission gun) and analyzed with energy dispersive X-ray spectroscopy (EDS, Tracor analyzer).

2.2.2 X-ray fluorescence, diffraction, and absorption spectroscopy

The Zn:Mn and Ca:Mn ratios were measured with an Eagle III μ-XRF spectrometer (Röntgenanalytik Messtechnik GmbH) equipped with a Rh anode and a 40 μm poly-capillary. The spectrometer was operated under vacuum at 20 kV and 400 μA, and fluorescence was measured for 300 s per point. Micro XRF, XRD and EXAFS data were collected on beamline 10.3.2 at the Advanced Light Source (ALS, Berkeley – Marcus et al., 2004a). Short root fragments were attached to the tips of glass capillaries and cooled down to 110-150 K (Oxford CryoSystems Cryo-Stream) to minimize radiation damage (Manceau et al., 2002b). X-ray fluorescence maps were taken at 10 keV incident energy, with a beam size ranging from 5×5 μm to 16×7 μm (H×V). Fluorescence counts were collected for K, Ca, Mn, Fe and Zn with a seven-element Ge solid-state detector and a counting time of 100 ms per pixel. For μ-EXAFS measurements, the vertical beam size ranged from 5 to 7 μm. A maximum of two spectra per precipitate were taken at either the Mn or the Zn K-edge to prevent the reduction of tetravalent to divalent Mn and the increase of structural disorder under the beam (Manceau et al., 2002b). Diffraction data were collected with a CCD camera (Bruker SMART6000, SMART software) at 17 keV (λ = 0.729 Å) and exposure times of 120-240 seconds. At this energy, the incident flux and absorption cross-sections are low enough to make radiation damage during an exposure negligible even at room temperature. A background pattern was

recorded next to each precipitate to subtract the scattering contribution from the root so as to obtain the precipitate pattern. Diffraction patterns collected on different precipitates were all statistically identical, and thus summed up to optimize data quality. Calibration of the energy and camera distance were obtained using an Al_2O_3 standard and Fit2D software (Hammersley, 1998). This software was also used to calculate the one-dimensional XRD traces from the radial integration of the two-dimensional patterns.

2.2.3 Data processing

The EXAFS data were analyzed according to standard procedure (Teo, 1986; Marcus et al., 2004b). The μ-XRD patterns were simulated following the trial-and-error approach developed by Drits and Tchoubar (1990), and applied previously to natural and synthetic phyllomanganates (Chukhrov et al., 1985; Manceau et al., 1997; Drits et al., 1998; Lanson et al., 2000, 2002a, b; Gaillot et al., 2003, 2005, 2007; Villalobos et al., 2006). Details on the program and fitting procedure can be found in the articles by Drits et al. (1998) and Plançon (2002). The scattering background was considered to be linear in the 0.35-0.80 $Å^{-1}$ $1/d$ interval (2.86-1.25 Å). The fit quality was evaluated over this interval using the conventional R_{WP} and R_{Exp} values (Howard and Preston, 1989).

3. RESULTS AND INTERPRETATION

3.1 Optical and electron microscopy

Under the optical microscope, the Mn-Zn precipitates appear as black stains about ten to several tens of micrometers in size on the root surface (Fig. 1a, EA-1). They are also observed in backscattered electron microscopy (Fig. 1b) due to the presence of high-Z elements (Mn, Zn, Ca, and minor Pb), but always are hardly noticeable in secondary electron

imaging mode (Fig. 1c). This suggests that the precipitates are engulfed in the root epidermis (Cotter-Howells et al., 1999) and do not coat the root surface as iron and manganese plaques do (Otte et al., 1989; St-Cyr and Campbell, 1996). No differences were observed among precipitates from plants grown in the untreated and mineral amended sediments. This result, together with the compartmentation of the precipitates inside the roots, suggests a biological origin. This interpretation is supported also by the absence of Zn-rich phyllomanganates in the surrounding soil matrix (Panfili et al., 2005).

3.2 Micro-XRF

Elemental mapping of *F. rubra* roots shows that Zn is associated with Mn in localized spots, and uniformly distributed without manganese in the vascular cylinder as expected for this nutritive element (Fig. 2 – Rout and Das, 2003). All roots have Zn in their central stele, but not all are speckled with Mn-Zn precipitates. Some root fragments are partly covered by Zn-free Fe-rich plaques (Fig. EA-2). These plaques are made of ferric oxyhydroxides, as indicated by their optical rusty color (Fig. 1a top right). In Zn-Mn-Ca tricolor representation all Mn-Zn precipitates generally have the same color (Fig. 2), even among different roots (Fig. EA-2), meaning that the relative proportions of Zn, Mn and Ca are about the same. The correlation coefficient between Zn and Mn counts for the precipitates is 0.8, with P-value < 0.0001 for the Anova F-test (Fig. 2). The Zn:Mn atomic ratio was calculated from the relative absorption jumps measured at the Mn and Zn K-edges on four particles. For each particle, a pre-absorption edge background was removed first, and then a linear fit to the post-edge region was extrapolated back to the edge to measure edge jumps. The ratio of the Zn to Mn edge jumps is 0.310(7), which translates into a Zn:Mn ratio of 0.46(1) when taking into account the atomic absorptions of the two elements. A consistent 0.44 value was obtained independently with the Eagle III spectrometer. This analysis also

confirmed that root precipitates have a constant Ca:Mn ratio. An atomic ratio of 0.41 was calculated after correction of the Ca-fluorescence from the root.

3.3 Micro-EXAFS spectroscopy

The Mn and Zn μ-EXAFS spectra for all precipitates were indistinguishable from each other, and thus averaged to improve the signal-to-noise ratio. If the precipitates consisted of an assemblage of distinct Zn and Mn species, the proportions of these species would most likely vary among the analyzed grains, and this variability would be detected by μ-EXAFS (Panfili et al., 2005). However, this was not the case, suggesting that all root precipitates consist of a single species, hereafter referred to as "Mn-Zn precipitate", in agreement with μ-XRF data.

3.3.1 Mn-EXAFS in Mn-Zn precipitate

Fig. 3 compares the EXAFS spectrum of Mn-Zn precipitate with those of reference compounds. The references used are hollandite (Hol) and todorokite (Todo), two tectomanganates with 2×2 (Hol) and 3×3 (Todo) tunnel structures, TcBi, a triclinic birnessite with 31% Mn^{3+} in the layers, $[Na^{+}_{0.31}(H_2O)_{0.40}(Mn^{4+}_{0.69}Mn^{3+}_{0.31})O_2$ – (Silvester et al., 1997; Lanson et al., 2002a)], Lit, a synthetic lithiophorite $[(Al_{0.67}Li_{0.32})(Mn^{4+}_{0.68}Mn^{3+}_{0.32})O_2(OH)_2$ – (Manceau et al., 2005)], HBi, a hexagonal birnessite prepared by equilibrating TcBi at pH 4 $[H^{+}_{0.33}Mn^{2+}_{0.043}Mn^{3+}_{0.123}(OH)^{-}_{0.013}(Mn^{4+}_{0.722}Mn^{3+}_{0.111}Vac_{0.167})O_2$ – (Silvester et al., 1997; Lanson et al., 2000)], chalcophanite (Chalco), a Zn-rich phyllomanganate with one in seven octahedral sites vacant and capped on each side of the surface layer by interlayer octahedral Zn atoms $[ZnMn_3O_7{\bullet}3H_2O$ – (Wadsley, 1955)], and dBi, a turbostratic birnessite with no interlayer Mn and no layer Mn^{3+} $[Na^{+}_{0.24}(H_2O)_{0.72}(Mn^{4+}_{0.94}Vac_{0.06})O_2$ – (Villalobos et al.,

185 2006)]. TcBi and Lit have a similar content of layer Mn^{3+}, but different Mn^{4+}-Mn^{3+} cation
186 ordering (Drits et al., 1997; Manceau et al., 2005).

187 Mn-Zn precipitate is not a tectomanganate because i) the second EXAFS oscillation
188 of tectomanganates is split or has a shoulder at 6.5 $Å^{-1}$, depending on the tunnel size
189 (Manceau and Combes, 1988; Mckeown and Post, 2001; Manceau et al., 2007b), and ii) their
190 [7.3-9.5 $Å^{-1}$] indicator region (Marcus et al., 2004b) does not match the data (Figs. 3a-b). In
191 the indicator region, Mn-Zn precipitate has a single maximum at 8.0-8.1 $Å^{-1}$ like dBi, HBi,
192 and Chalco. The shape and position of this maximum is diagnostic of Mn^{4+}-rich manganate
193 layers with hexagonal symmetry (Gaillot et al., 2007). For example, this maximum is shifted
194 to 7.9 $Å^{-1}$ (i.e., consistent with longer distances) in Lit (Manceau et al., 2004) due to the large
195 amount of Mn^{3+} in the hexagonal layer. TcBi has a distinctive double peak with a minimum at
196 7.9-8.0 $Å^{-1}$ as a result of the split of the Mn-Mn distances induced by the linear ordering of
197 Mn^{3+} and Mn^{4+} cations in the layer (Drits et al., 1997; Lanson et al., 2002a; Gaillot et al.,
198 2003, 2007; Manceau et al., 2005). This cation ordering lowers the layer symmetry from
199 hexagonal to orthogonal. Thus, the Mn-Zn precipitate is a phyllomanganate having hexagonal
200 layer symmetry and little layer Mn^{3+}. The subtle differences between Mn-Zn precipitate and
201 some phyllomanganate references are more obvious when the data are Fourier transformed
202 (FT, Fig. 4). The phase of the $Mn1_E$ peak matches those of dBi, Chalco, and HBi, and is
203 shifted to a shorter distance relative to Lit. In phyllomanganates, the $Mn1_E$ peak represents
204 Mn atoms in the first-neighbor layer octahedra (Manceau and Combes, 1988). Therefore, its
205 phase depends on the nearest Mn-Mn distance (Mn-Mn1 pair), and is sensitive to the amount
206 of Mn^{3+} in the layer similarly to the phase of the O peak. However, the sensitivity of the phase
207 of this peak to the presence of Mn^{3+} is not high enough to distinguish HBi (11% layer Mn^{3+}
208 per octahedral site) from dBi and Chalco (0% – Fig. EA-3). The $Mn3_E$ peak is twice as
209 sensitive as the $Mn1_E$ peak because it arises from the third-neighbor octahedra at twice the

Mn-Mn1 distance (see for example Fig. 11 in Manceau et al., 2005). The sensitivity is now high enough to differentiate HBi from dBi and Chalco, as shown in Fig. 4. Thus, using the phase of the $Mn1_E$ and $Mn3_E$ peaks as chemical probes to the layer composition, we conclude that Mn-Zn precipitate has less Mn^{3+} in the octahedral layers than HBi (11%), if any. Confirming evidence is found in the comparison of the frequency of EXAFS spectra. Fig. 3 shows that the overall EXAFS frequency, and hence interatomic distances, increase from dBi/Chalco/Mn-Zn precipitate, to HBi, to Lit/TcBi, as a result of the increasing amount of layer Mn^{3+} (Gaillot et al., 2007).

In contrast to the Mn1 peak, the phase of the O peak (i.e., average Mn-O distance in the layer and interlayer) matches those of the two Mn^{3+}-free references (dBi, Chalco) and is slightly shifted to lower distance relative to both HBi and Lit. This shift is barely visible in Fig. 4, but clearly apparent when the [1-3 Å] $R+\Delta R$ interval is expanded (Fig. EA-3). Thus, Mn-Zn precipitate has no detectable Mn^{3+} in the layer similarly to dBi and Chalco, nor in the interlayer, in contrast to HBi.

The FT of Mn-Zn precipitate also differs from that of HBi by the absence of the $Mn1_{TC}$ peak from Mn_{layer}-Me pairs at ~3.5 Å ($R + \Delta R \sim 3.1$ Å), where Me is an interlayer metal cation, such as Mn, Zn, or Pb, in triple-corner sharing position above or below vacant layer sites (TC linkage – Manceau et al., 2002a). When there are interlayer Mn atoms, this peak is intense because each interlayer Mn is surrounded by as many as six Mn_{layer} neighbors. In contrast, Mn_{layer} atoms near an octahedral vacancy have fewer interlayer Mn neighbors, their exact number depending on the density of layer vacancies and composition of the interlayer. Here, the lack of $Mn1_{Tc}$ peak in Mn-Zn precipitate suggests that it has no detectable Me cations on either side of the layer vacancies. The $Mn5_E$ peak is also absent in the FT of Mn-Zn precipitate, as in dBi, but not HBi nor Chalco. This peak arises from the 5th Mn shell at about $2.90 \times 3 = 8.7$ Å, and is enhanced by forward scattering from two

intervening Mn_{layer} (Manceau et al., 2005). The absence of this peak in Mn-Zn precipitate indicates that the octahedral layers have a small lateral dimension. This peak is also absent in Lit, but in this case because the Mn-Mn5 shell is split as a result of the Mn^{4+}-Mn^{3+} ordering in the layer (Manceau et al., 2005).

3.3.2 Zn-EXAFS in Mn-Zn precipitate

The best spectral match of Mn-Zn precipitate to our Zn species database was obtained with tetrahedrally coordinated Zn (^{IV}Zn) sorbed above/below octahedral vacancies of a phyllomanganate (^{IV}TC site – Fig. 5a). This Zn complex is common in nature and its local structure has been described previously (Manceau et al., 2000b, 2002a; Marcus et al., 2004b; Isaure et al., 2005; Toner et al., 2006). Although the ^{IV}Zn-sorbed phyllomanganate reference provides a good approximation of Zn local structure in Mn-Zn precipitate, there are significant differences between the two spectra, particularly in the phase mismatches between 6.5 and 10 $Å^{-1}$, and the symmetry of the first and second oscillations. These differences have been documented previously and result from the mixed occupancy of the TC site by tetrahedral and octahedral Zn (Manceau et al., 2002a, 2007b). Adding the chalcophanite or $^{VI/IV}$Zn-sorbed dBi reference (Fig. 5b – Toner et al., 2005a, 2006) in a two-component linear fit to the data compensated for the phase shift and asymmetry of the first oscillation, but not entirely for that of the second (Fig. 5c). All attempts to suppress this residual by adding a third component to the linear fit failed. Therefore, although there is some uncertainty on the exact configuration of the minor ^{VI}Zn site, the ^{IV}TC + ^{VI}TC model is the best description of the data we can offer. Consideration of an edge-sharing complex (^{VI}TE) at layer edges did not reproduce the phase as well as the ^{VI}TC surface species. The ^{VI}TC species may occur also at the edge of the Mn-Zn precipitate layer, instead of the basal surface, in which case it has a slightly different binding environment from that of dBi. Thus, the dBi and chalcophanite

standards may not be the best proxies for the ^{VI}TC species. The fraction of each Zn species derived from the two-component least-squares fit is 87 ± 10% ^{IV}TC and 27 ± 10% ^{VI}TC.

3.3.3 Zn-EXAFS in Zn-only precipitate

A few spots in the μ-XRF maps contained Zn and little else detectable. EXAFS spectroscopy identified zincite (ZnO) and sphalerite (ZnS), two mineral species originally present in the untreated sediment (Isaure et al., 2002). These grains are likely residual slag material stuck to the root surface that were not removed by washing. None of the Zn species formed in the rhizosphere of *F. rubra* after the two years of experiment were detected in or at the root surface.

3.3.4 Zn-EXAFS in the root vascular cylinder

Micro-EXAFS spectra were recorded in the vascular cylinder of four distinct roots, at spots containing little Mn. All spectra were indistinguishable, indicating that Zn speciation is uniform, and thus averaged. The resulting Root spectrum has the same frequency as the Mn-Zn precipitate spectrum, which suggests that Zn is also mostly tetrahedral in the roots (Fig. 5d). However, in contrast to Mn-Zn precipitate, the second and third oscillations of the Root spectrum are not split, indicative of "light" backscatters from second-shell contributions. Consistently, the best spectral match to our organic and inorganic database of the Root spectrum was provided with Zn in a biofilm (Zncell7, Fig. 5e). This reference has 80 ± 10% Zn complexed to phosphoryl groups and 20 ±10% to carboxyl groups (Toner et al., 2005b). Consistent with this other study, consideration of carboxyl (citrate, Fig. 5f) and phosphate (phytate, Fig. 5g; Zn-sorbed *Penicillium chrysogenum,* Fig. 5h – Sarret et al., 1998a) ligands alone, did not yield an optimal fit to the data. Zinc preferential binding to phosphate groups has been reported also in the roots of *Arabidopsis halleri* and *A. lyrata* grown hydroponically,

on bacterial and fungi cells, and in biofilms (Sarret et al., 1998b, 2002; Fein et al., 2001). These studies have shown that Zn has a higher affinity for phosphate than for carboxyl groups, which is consistent with the predominance of the phosphate species in *F. rubra* roots.

3.4 Micro-XRD

3.4.1 Qualitative description of the data

According to μ-XRF and μ-EXAFS, Mn-Zn precipitate is a phyllomanganate with hexagonal layer symmetry, little to no layer Mn^{3+}, less interlayer Mn^{3+} than HBi, and as much as 0.46 interlayer Zn per total Mn, of which 87 ± 10% is tetrahedral and 27 ± 10% octahedral. Despite its lamellar structure, the XRD pattern of Mn-Zn precipitate shows no patent basal reflections (Fig. 6). The XRD trace is dominated by two reflections at ~2.45 and ~1.42 Å, the first one being asymmetric towards higher $1/d$ values. This profile is characteristic of lamellar compounds with turbostratic stacking, i.e., lacking well-defined displacement/rotation between successive layers (Warren, 1941; Biscoe and Warren, 1942; Brindley, 1980). The positions, profiles, and relative intensities of the two peaks match the [20,11] and [02,31] scattering bands of turbostratic birnessite, choosing a C-centered cell for their crystallographic assignment (Drits et al., 1997, 2007; Villalobos et al., 2006). Their *d*-spacings are in the ratio of 1.73, close to the √3 value for hexagonal symmetry. Their profiles are controlled by the structure factor and can thus be used for structural determinations (Villalobos et al., 2006; Drits et al., 2007), as shown below.

3.4.2 Simulation of the 0.35-0.80 Å^{-1} 1/d interval

XRD simulations were performed with the C-centered unit-cell parameters b = 2.850 Å, $a = b\sqrt{3}$ = 4.936 Å, γ = 90° derived from the position of the [20,11] and [02,31] bands, $d_{(001)}$ = 7.20 Å, and a random layer stacking (Wr = 100%, Fig. EA-4). The atomic

coordinates for the ^{IV}TC and ^{VI}TC sites were considered to be the same as those in Zn-sorbed birnessite (Table 1 – Lanson et al., 2002b). The Ca position was assumed to be close to that in Ca-rich birnessite (Drits et al., 1998), that is in the mid-plane of the interlayer almost above a tetrahedral surface site (TE position – Fig. EA-5). Thus, parameters optimized in the simulations are the amount of vacant layer sites, the amount, position, and coordination of interlayer Zn^{2+} and $Mn^{2+,3+}$, the *xy* coordinates of Ca^{2+}, the position of water molecules, and the size of the coherent scattering domains (CSDs) in the *ab* plane. The CSDs were considered to have a disk-like shape, whose average radius was constrained by fitting the maximum at ~2.45 Å (Villalobos et al., 2006).

Since the phyllomanganate has 0.46 interlayer Zn per total Mn, at least 0.186 vacant layer sites per octahedron are needed to accommodate all Zn [(0.186 × 2) / (1.00 - 0.186) = 0.46]. In this case, every vacant site is capped by one Zn on either side. No satisfactory agreement between theory and experiment could be obtained with this model, regardless of the amount and position of Ca^{2+}. In particular, the high 1/*d* tail of the [20,11] band at ~0.43-0.45 $Å^{-1}$ was poorly reproduced (Fig. 7a – R_{WP} = 3.57%; R_{Exp} = 1.57%). To reproduce this feature it was necessary to increase the density of vacant sites to 0.22, and thus to introduce interlayer Mn in TC and TE sites to keep the Zn:Mn ratio constant. Our best theoretical model to the data is shown in Fig. 7b (R_{WP} = 3.49%; R_{Exp} = 1.57%), and structural parameters are listed in Tables 1 and 2. The structural formula is $[(Mn_{0.78}Vac_{0.22})O_2]^{TC}Mn_{0.010}{}^{TE}Mn_{0.046}{}^{VI}Zn_{0.088}{}^{IV}Zn_{0.300}Ca_{0.318}(H_2O)_{0.972}]$, and the structure model is schematized in Figs. 8 and EA-5. The refined model contains 0.38 Ca per Mn, in agreement with μ-XRF data (0.41), at a position [(-0.410, 0, ½) and symmetric positions] slightly shifted from the ideal TE position [(-0.333, 0, ½) – Fig. EA-5]. Interlayer H_2O molecules that are not bound to Zn and interlayer Mn are located in (0.220, 0, ½) and symmetric positions. This position is similar to ordered (Lanson et al., 2002a) and disordered

(Villalobos et al., 2006) Na-exchanged birnessite varieties. It allows for the formation of strong H-bonds with O_{layer} atoms [d(O_{layer}-$H_2O_{inter.}$) = 2.66 Å, Table 2]. Overall, only the Mn TE position is new, all others have been described previously for other birnessite varieties.

3.4.3 Sensitivity of calculated XRD patterns to structural parameters

As the optimal fit to data was obtained using a trial-and-error approach, the sensitivity of the XRD simulations to key structural parameters needs to be assessed. A key parameter for birnessite's ability to sorb trace metals is the origin of the layer charge. In the present model, the layer charge arises from layer vacancies only, not at all from substitution of Mn^{3+} for Mn^{4+} in the layer, because the hexagonal layer symmetry and small *b* unit-cell dimension (2.85 Å) are incompatible with appreciable amount of Mn^{3+} in the layer (Gaillot et al., 2005, 2007; Manceau et al., 2005). When birnessite contains ~25% layer Mn^{3+} per octahedral site with the long Mn-O bonds oriented at random, *b* = 2.895 Å (Gaillot et al., 2007) and the [20,11] and [02,31] bands are shifted to lower 1/*d* values relative to data (R_{WP} = 7.15%; Fig. 7c). Mn-Zn precipitate has the same *b* value as HBi (2.850 Å) which contains 11% layer Mn^{3+} per octahedral site (Lanson et al., 2000). Based on EXAFS results, this amount is regarded as an upper limit. Also, if the layer contained a high proportion of Mn^{3+} cations ordered in rows, as in triclinic birnessite, a similar *b* value (2.84-2.85 Å) would be measured but the [02,31] band would be a doublet due to the departure from hexagonal symmetry (Drits et al., 2007; Gaillot et al., 2007). Calculations show that the band splitting decreases with the layer dimension, but that it should still be observed for a CSD dimension of 33 Å, the optimal CSD value (Fig. 7d – R_{WP} = 6.79%).

The sensitivity of XRD profiles to the amount, coordination, and position of high-Z interlayer scatterers, and to the number of vacant layer sites is illustrated next. If interlayer Mn atoms are located only in ^{VI}TC sites (0.056 per octahedron) rather than distributed over

^{VI}TE and ^{VI}TC sites (0.046 and 0.010, respectively), the dip at ~0.52 Å^{-1} is deeper and the intensity of the broad hump at ~0.60 Å^{-1} is increased (Fig. 7e – R_{WP} = 3.60%). When the number of interlayer Ca^{2+} is decreased from 0.318 to 0.240, there is a deficit of intensity in the 0.43-0.45 Å^{-1} region (Fig. 7f – R_{WP} = 3.54%). Similarly, decreasing the number of interlayer Zn from 0.388 to 0.244, and that of vacant layer sites from 0.22 to 0.15 broadens the high 1/*d* tail of the [20,11] band and shifts the hump at ~0.60 Å^{-1} to lower 1/*d* values (Fig. 7g – R_{WP} = 4.92%). Increasing the proportion of octahedrally coordinated interlayer Zn from 23% to 50% also broadens the high 1/*d* tail of the [20,11] band and increases the intensity of the broad hump at ~0.60 Å^{-1} (Fig. 7h – R_{WP} = 3.99%). Finally, the sensitivity of XRD profiles to ^{IV}Zn, ^{VI}Zn, and Ca coordinates is shown in Figure EA-6.

3.4.4 Simulation of the 0.05-0.35 Å^{-1} 1/d interval

Despite the lamellar structure of Mn-Zn precipitate, its XRD pattern lacks well-defined 00*l* reflections. To assess the possible origin of this oddity, the 001 and 002 reflections were calculated for crystallites with extremely small CSD dimension along the *c** axis (Fig. 9). Calculations show that at least two layers are required to modulate the scattering profile at low 1/*d* values, otherwise the X-ray intensity steadily decreases with increasing 1/*d* (Fig. 9). The best fit to data was obtained with a mixture of crystallites containing 1, 2, and 3 layers in the ratio of 20:3:1, respectively, leading to an average CSD dimension along the *c** axis of 1.2 layers (~8.6 Å).

4. DISCUSSION

4.1 Structure model

4.1.1 Amount of vacant sites and Zn loading

Except for one sample obtained by metal sorption on poorly crystalline Mn oxides (Nelson et al., 1999), the new Zn-rich phyllomanganate contains higher amounts of vacant layer sites (0.22 per layer octahedron) and transition elements (0.44 total Mn and Zn per layer octahedron) than any other natural and synthetic variety described so far (0.167 and 0.22, respectively; Lanson et al., 2000, 2002b; Villalobos et al., 2006). The constant Zn:Mn ratio of Mn-Zn precipitate suggests that Zn co-precipitated with Mn by a yet unknown mechanism to form a chemically well-defined phase as natural solids formed by metal sorption on pre-existing mineral surfaces are chemically heterogeneous (see for example Manceau et al., 2007b).

4.1.2 Presence of heavy scatterers above and below vacant layers sites

According to XRD and Zn-EXAFS, Mn-Zn precipitate has 0.300 ^{IV}Zn and 0.088 ^{VI}Zn per octahedron in TC position (Table 1). The Zn-Mn pairs are detected at the Zn K-edge (Fig. EA-7) but not at the Mn K-edge for two possible reasons. In a vacancy-free layer, each Mn has six nearest-neighbor Mn atoms. In Mn-Zn precipitate, this number is 4.25 if two vacancies cannot be adjacent which is always the case in layered structures (Manceau et al., 2000a). Thus, each Mn octahedron is surrounded statistically by 1.75 vacant sites. With 80% of these vacant sites capped by Me cations on both sides, and 20% on one side only, Mn_{layer} atoms are coordinated on average to $1.75 \times (0.2 + (0.8 \times 2)) = 3.15$ Me in TC sites. This number is about half the value for Zn, as each Zn is linked to six Mn_{layer}. Structural disorder also can be invoked to explain the absence of Mn-Zn pairs in Mn-EXAFS. The TC position is occupied by at least three types of complex: 0.300 ^{IV}Zn, 0.088 ^{VI}Zn, and 0.010 ^{VI}Mn, and the TE position by 0.046 Mn. Each Mn_{layer}-$^{(TC,TE)}$Me pair has a different distance, and this broad distribution results in an apparent loss of coordination.

4.2 Intensity of basal reflections

Birnessite and vernadite minerals were given different names because the basal reflections of birnessite at 7.2-7.0 Å (001) and 3.6-3.5 Å (002) were not observed originally in the diffraction pattern of vernadite (Chukhrov and Gorshkov, 1980; Chukhrov et al., 1980). However, recent studies have shown that natural vernadite and its biogenic and chemical (δ-MnO_2) analogs most often display a 001 reflection when their XRD pattern is recorded on modern diffractometers (Mandernack et al., 1995; Villalobos et al., 2003, 2005; Jurgensen et al., 2004; Webb et al., 2005b; Bodeï et al., 2007; Manceau et al., 2007a, b), thus confirming the view of Arrhenius et al. (1978) and Giovanoli (1980) that this mineral is a *c*-disordered variety of birnessite. Villalobos et al. (2006) showed that basal reflections are present when the diffracting crystallites have only 2-3 layers, on average. Here, this number is as low as 1.2 layers, meaning that Mn-Zn precipitate is essentially an assemblage of isolated layers. Measurements of the Mn edge jumps on different Mn-Zn precipitates provide an inkling of how the constitutive nanoparticles are joined at particle or so-called grain boundaries. The Mn edge jump was typically between 0.2 and 0.3 for aggregates ~15-25 μm in diameter, which indicates that the phyllomanganate represents only a small fraction (~20 volume %) of the black precipitates, thus revealing a high micro-porosity. This porosity is possibly filled, at least partly, by organics that may help disrupt the parallelism of the layers, but also to tie them together.

4.3 Biologically induced oxidation of manganese

Many microorganisms have the capacity to oxidize and precipitate Mn as manganate (Tebo et al., 2004, and references therein). Since biological oxidation of Mn is generally faster than abiotic oxidation, most natural Mn oxides are considered to be biogenic.

Pseudomonas putida (Villalobos et al., 2003, 2006; Toner et al., 2005a), *Leptothrix discophora* (Nelson et al., 1999, 2002; Nelson and Lion, 2003; Jurgensen et al., 2004; Saratovsky et al., 2006), and *Bacillus* sp. strain SG-1 (Mandernack et al., 1995; Tebo et al., 1998; Webb et al., 2005a, b) are the three fairly-well characterized bacterial model systems for the oxidation of manganese in the environment. Manganese oxidation and the subsequent precipitation of Mn(III,IV) bioxides by microscopic fungi is also well documented (Krumbein and Jens, 1981; Emerson et al., 1989; Schulze et al., 1995; Tani et al., 2003, 2004; Miyata et al., 2004, 2006a, b; Thompson et al., 2005). Here, we showed that Mn can be biomineralized also in higher living organisms, such as plants. Except for its atypical high Zn content and the structural consequences thereof, this new manganese biomineral is no exception to the intrinsic nanocrystalline nature of biogenic phyllomanganates.

Although the mechanism of Mn(II) to Mn(IV) oxidation is presently unknown, the constant Zn:Mn ratio of the new Mn biooxide suggests the existence of a well-defined bioactive process, likely in response to metal toxicity. The occurrence of Zn-Mn precipitate only in the root epidermis and the absence in the roots of any Zn-rich species from the soil matrix (Panfili et al., 2005) suggest that Mn oxidation did not occur in the rhizosphere, and thus does not result from bacterial activity or abiotic reaction. Divalent manganese may have been complexed and transported to the roots by phytosiderophores (Römheld, 1991), and then oxidized by the plant itself or by endomycorrhizal fungi, as shown for wheat and soybean (Schulze et al., 1995; Thompson et al., 2005, 2006).

Knowing how to stimulate the formation of this new phase in biological systems, or how to synthesize it abiotically, would be a significant progress towards Zn immobilization in contaminated environments and their (phyto-)remediation. Formation of this new phase could in particular facilitate the growth of plants in highly contaminated environments in lowering the concentration of bio-available Zn in the rhizosphere.

ACKNOWLEDGMENTS

The following persons are thanked for their contribution on various aspects of this work: Fabienne Marseille and Bertrand Girondelot (CNRSSP, Douai) for the setup of pot experiments, Clément Falk (LGIT, Grenoble) for optical microscopy on Mn-Zn precipitate, Serge Nitsche, Damien Chaudanson, and Alain Baronnet (CRMCN, Marseilles) for SEM analysis, Manuel Muñoz (LGCA, Grenoble) for XRF measurements on the Eagle spectrometer, Didier Arnal, Nicole Paoletti, and Gérard Souche (R&S, Montpellier) for growing *Festuca rubra* in hydroponic conditions, and Benoît Jaillard and Philippe Hinsinger (R&S, Montpellier) for fruitful discussions about metal uptake by plants. This research was supported by the ACI/FNS Ecco (EcoDyn) program. The ALS is supported by the Director, Office of Energy Research, Office of Basic Energy Sciences, Materials Sciences Division of the U.S. Department of Energy, under Contract No. DE-AC02-05CH11231.

REFERENCES

Arrhenius G., Cheung K., Crane S., Fisk M., Frazer J., Korkisch J., Melin T., Nakao S., Tsai A., and Wolf G. (1978) Counterions in marine manganates. In *La genèse des nodules de manganèse* (ed. C. Lalou). Proc. Int. Coll. CNRS **289**, 333-356.

Biscoe J. and Warren B.E. (1942) An X-ray study of carbon black. *J. App. Phys.* **13**, 364-371.

Bodeï S., Manceau A., Geoffroy N., Baronnet A., and Buatier M. (2007) Formation of todorokite from vernadite in Ni-rich hemipelagic sediments. *Geochim. Cosmochim. Acta* **71**, in press.

Brese N.E. and O' Keeffe M. (1991) Bond-valence parameters for solids. *Acta Crystallogr.* **B47**, 192-197.

Brindley G.W. (1980) Order-disorder in clay mineral structures. In *Crystal Structures of Clay Minerals and their X-ray Identification* (ed. G.W. Brindley and G. Brown), pp. 125-195. Mineralogical Society.

Chukhrov F.V. and Gorshkov A.I. (1980) Reply to R. Giovanoli's comment. *Miner. Depos.* **15**, 255-257.

Chukhrov F.V., Gorshkov A.I., Rudnitskaya E.S., Berezovskaya V.V., and Sivtsov A.V. (1980) Manganese minerals in clays: A review. *Clays & Clay Miner.* **28**, 346-354.

Chukhrov F.V., Sakharov B.A., Gorshkov A.I., Drits V.A., and Dikov Y.P. (1985) Crystal structure of birnessite from the Pacific ocean. *Int. Geol. Rev.* **27**, 1082-1088.

Cotter-Howells J.D., Champness P.E., and Charnock J.M. (1999) Mineralogy of Pb-P grains in the roots of *Agrostis capillaris* L. by ATEM and EXAFS. *Miner. Mag.* **63**, 777-789.

Cunningham S.D., Berti W.R., and Huang J.W. (1995) Phytoremediation of contaminated soils. *Trends Biotech.* **13**, 393-397.

Drits V.A. and Tchoubar C. (1990) *X-ray diffraction by disordered lamellar structures: Theory and applications to microdivided silicates and carbons*. Springer-Verlag.

Drits V.A., Silvester E.J., Gorshkov A.I., and Manceau A. (1997) The structure of monoclinic Na-rich birnessite and hexagonal birnessite. Part 1. Results from X-ray diffraction and selected area electron diffraction. *Amer. Mineral.* **82**, 946-961.

Drits V.A., Lanson B., Gorshkov A.I., and Manceau A. (1998) Substructure and superstructure of four-layer Ca-exchanged birnessite. *Amer. Mineral.* **83**, 97-118.

Drits V.A., Lanson B., and Gaillot A.C. (2007) Birnessite polytype systematics and identification by powder X-ray diffraction. *Amer. Mineral.* **92**, 771-788.

Emerson D., Garen R.E., and Ghiorse W.C. (1989) Formation of *Metallogenium*-like structures by a manganese-oxiding fungus. *Arch. Microbiol.* **151**, 223-231.

Fein J.B., Martin A.M., and Wightman P.G. (2001) Metal adsorption onto bacterial surfaces: Development of a predictive approach. *Geochim. Cosmochim. Acta* **65**, 4267-4273.

Gaillot A.-C., Flot D., Drits V.A., Manceau A., Burghammer M., and Lanson B. (2003) Structure of synthetic K-rich birnessite obtained by high-temperature decomposition of $KMnO_4$. I. Two-layer polytype from 800°C experiment. *Chem. Mater.* **15**, 4666-4678.

Gaillot A.-C., Lanson B., and Drits V.A. (2005) Structure of birnessite obtained from decomposition of permanganate under soft hydrothermal conditions. 1. Chemical and structural evolution as a function of temperature. *Chem. Mater.* **17**, 2959-2975.

Gaillot A.-C., Drits V.A., Manceau A., and Lanson B. (2007) Structure of the synthetic K-rich phyllomanganate birnessite obtained by high-temperature decomposition of KMnO4 - Substructures of K-rich birnessite from 1000°C experiment. *Micropor. Mesopor. Mater.* **98**, 267-282.

Giovanoli R. (1980) Vernadite is random-stacked birnessite. *Mineral. Depos.* **15**, 251-253.

Hammersley A.P. (1998) FIT2D V9.129 - Reference manual V3.1, Vol. 346. ESRF internal report - ESRF98HA01T.

Howard S.A. and Preston K.D. (1989) Profile fitting of powder diffraction patterns. In *Modern Powder Diffraction*, Vol. 20 (ed. D.L. Bish and J.E. Post), pp. 217-275. Mineralogical Society of America.

Isaure M.P., Laboudigue A., Manceau A., Sarret G., Tiffreau C., Trocellier P., Lamble G., Hazemann J.L., and Chateigner D. (2002) Quantitative Zn speciation in a contaminated dredged sediment by μ-PIXE, μ-SXRF, EXAFS spectroscopy and principal component analysis. *Geochim. Cosmochim. Acta* **66**, 1549-1567.

Isaure M.P., Manceau A., Geoffroy N., Laboudigue A., Tamura N., and Marcus M.A. (2005) Zinc mobility and speciation in soil covered by contaminated dredged sediment using micrometer-scale and bulk-averaging X-ray fluorescence, absorption and diffraction techniques. *Geochim. Cosmochim. Acta* **69**, 1173-1198.

Jurgensen A., Widmeyer J.R., Gordon R.A., Bendell Young L.I., Moore M.M., and Crozier E.D. (2004) The structure of the manganese oxide on the sheath of the bacterium *Leptothrix discophora*: An XAFS study. *Amer. Mineral.* **89**, 1110-1118.

Krämer U. (2005) Phytoremediation: novel approaches to cleaning up polluted soils. *Curr. Opin. Biotechnol.* **16**, 133-141.

Krumbein W.E. and Jens K. (1981) Biogenic rock varnishes of the Negev Desert (Israel) an ecological study of iron and manganese transformation by cyanobacteria and fungi. *Oecologia* **50**, 25-38.

Lanson B., Drits V.A., Silvester E.J., and Manceau A. (2000) Structure of H-exchanged hexagonal birnessite and its mechanism of formation from Na-rich monoclinic buserite at low pH. *Amer. Mineral.* **85**, 826-838.

Lanson B., Drits V.A., Feng Q., and Manceau A. (2002a) Structure of synthetic Na-birnessite: Evidence for a triclinic one-layer unit cell. *Amer. Mineral.* **87**, 1662-1671.

Lanson B., Drits V.A., Gaillot A.-C., Silvester E., Plancon A., and Manceau A. (2002b) Structure of heavy-metal sorbed birnessite: Part 1. Results from X-ray diffraction. *Amer. Mineral.* **87**, 1631-1645.

Li Y.M., Chaney R.L., Siebielec G., and Kerschner B.A. (2000) Response of four turfgrass cultivars to limestone and biosolids-compost amendment of a zinc and cadmium contaminated soil at Palmerton, Pennsylvania. *J. Environ. Qual.* **29**, 1440-1447.

Ma M., Lau P.S., Jia Y.T., Tsang W.K., Lam S.K.S., Tam N.F.Y., and Wong Y.S. (2003) The isolation and characterization of Type 1 metallothionein (MT) cDNA from a heavy-metal-tolerant plant, *Festuca rubra* cv. Merlin. *Plant Sci.* **164**, 51-60.

Manceau A. and Combes J.-M. (1988) Structure of Mn and Fe oxides and hydroxides: A topological approach by EXAFS. *Phys. Chem. Miner.* **15**, 283-295.

Manceau A., Drits V.A., Silvester E.J., Bartoli C., and Lanson B. (1997) Structural mechanism of Co^{2+} oxidation by the phyllomanganate buserite. *Amer. Mineral.* **82**, 1150-1175.

Manceau A., Lanson B., Drits V.A., Chateigner D., Gates W.P., Wu J., Huo D., and Stucki J.W. (2000a) Oxidation-reduction mechanism of iron in dioctahedral smectites: I. Crystal chemistry of oxidized reference nontronites. *Amer. Mineral.* **85**, 133-152.

Manceau A., Lanson B., Schlegel M.L., Harge J.-C., Musso M., Eybert Berard L., Hazemann J.L., Chateigner D., and Lamble G.M. (2000b) Quantitative Zn speciation in smelter-contaminated soils by EXAFS spectroscopy. *Amer. J. Sci.* **300**, 289-343.

Manceau A., Lanson B., and Drits V.A. (2002a) Structure of heavy metal sorbed birnessite. Part III: Results from powder and polarized extended X-ray absorption fine structure spectroscopy. *Geochim. Cosmochim. Acta* **66**, 2639-2663.

Manceau A., Marcus M.A., and Tamura N. (2002b) Quantitative speciation of heavy metals in soils and sediments by synchrotron X-ray techniques. In *Applications of Synchrotron Radiation in Low-Temperature Geochemistry and Environmental Sciences*, Vol. 49, pp. 341-428.

Manceau A., Marcus M.A., Tamura N., Proux O., Geoffroy N., and Lanson B. (2004) Natural speciation of Zn at the micrometer scale in a clayey soil using X-ray fluorescence, absorption, and diffraction. *Geochim. Cosmochim. Acta* **68**, 2467-2483.

Manceau A., Tommaseo C., Rihs S., Geoffroy N., Chateigner D., Schlegel M., Tisserand D., Marcus M.A., Tamura N., and Chen Z.S. (2005) Natural speciation of Mn, Ni, and Zn at the micrometer scale in a clayey paddy soil using X-ray fluorescence, absorption, and diffraction. *Geochim. Cosmochim. Acta* **69**, 4007-4034.

Manceau A., Kersten M., Marcus M.A., Geoffroy N., and Granina L. (2007a) Ba and Ni speciation in a nodule of binary Mn oxide phase composition from Lake Baikal. *Geochim. Cosmochim. Acta* **71**, 1967-1981.

Manceau A., Lanson M., and Geoffroy N. (2007b) Natural speciation of Ni, Zn, Ba, and As in ferromanganese coatings on quartz using X-ray fluorescence, absorption, and diffraction. *Geochim. Cosmochim. Acta* **71**, 95-128.

Mandernack K.W., Post J., and Tebo B.M. (1995) Manganese mineral formation by bacterial spores of the marine *Bacillus*, strain SG-1: Evidence for the direct oxidation of Mn(II) to Mn(IV). *Geochim. Cosmochim. Acta* **59**, 4393-4408.

Marcus M.A., MacDowell A.A., Celestre R., Manceau A., Miller T., Padmore H.A., and Sublett R.E. (2004a) Beamline 10.3.2 at ALS: a hard X-ray microprobe for environmental and materials sciences. *J. Synchrotron Radiat.* **11**, 239-247.

Marcus M.A., Manceau A., and Kersten M. (2004b) Mn, Fe, Zn and As speciation in a fast-growing ferromanganese marine nodule. *Geochim. Cosmochim. Acta* **68**, 3125-3136.

McKeown D.A. and Post J.E. (2001) Characterization of manganese oxide mineralogy in rock varnish and dendrites using X-ray absorption spectroscopy. *Amer. Mineral.* **86**, 701-713.

Mench M., Bussiere S., Boisson J., Castaing E., Vangronsveld J., Ruttens A., De Koe T., Bleeker P., Assuncao A., and Manceau A. (2003) Progress in remediation and revegetation of the barren Jales gold mine spoil after in situ treatments. *Plant and Soil* **249**, 187-202.

Miyata N., Tani Y., Iwahori K., and Soma M. (2004) Enzymatic formation of manganese oxides by an *Acremonium*-like hyphomycete fungus, strain KR21-2. *FEMS Microbiol. Ecol.* **47**, 101-109.

Miyata N., Maruo K., Tani Y., Tsuno H., Seyama H., Soma M., and Iwahori K. (2006a) Production of biogenic manganese oxides by anamorphic ascomycete fungi isolated from streambed pebbles. *Geomicrobiol. J.* **23**, 63-73.

Miyata N., Tani Y., Maruo K., Tsuno H., Sakata M., and Iwahori K. (2006b) Manganese(IV) oxide production by *Acremonium sp.* strain KR21-2 and extracellular Mn(II) oxidase activity. *Appl. Environ. Microbiol.* **72**, 6467-6473.

Nelson Y.M., Lion L.W., Ghiorse W.C., and Shuler M.L. (1999) Production of biogenic Mn oxides by *Leprothrix discophora* SS-1 in a chemically defined growth medium and evaluation of their Pb adsorption characteristics. *Appl. Environ. Microbiol.* **65**, 175-180.

Nelson Y.M., Lion L.W., Shuler M.L., and Ghiorse W.C. (2002) Effect of oxide formation mechanisms on lead adsorption by biogenic manganese (hydr)oxides, iron (hydr)oxides, and their mixtures. *Environ. Sci. Technol.* **36**, 421-425.

Nelson Y.M. and Lion L.W. (2003) Formation of biogenic manganese oxides and their influence on the scavenging of toxic trace elements. *Geochemical And Hydrological Reactivity Of Heavy Metals In Soils*, 169-186.

Otte M.L., Rozema J., Koster L., Haarsma M.S., and Broekman R.A. (1989) Iron plaque on roots of *Aster tripolium* L.: Interaction with zinc uptake. *New Phytol.* **111**, 309-317.

Panfili F. (2004) Etude de l'évolution de la spéciation du zinc dans la phase solide d'un sédiment de curage contaminé induite par phytostabilisation. Ph.D. thesis, Univ. Aix-Marseille, France, .

Panfili F.R., Manceau A., Sarret G., Spadini L., Kirpichtchikova T., Bert V., Laboudigue A., Marcus M.A., Ahamdach N., and Libert M.F. (2005) The effect of phytostabilization on Zn speciation in a dredged contaminated sediment using scanning electron microscopy, X-ray fluorescence, EXAFS spectroscopy, and principal components analysis. *Geochim. Cosmochim. Acta* **69**, 2265-2284.

Plançon A. (2002) CALCIPOW- a program for calculating the diffraction by disordered lamellar structures. *J. Appl. Cryst.* **35**, 377.

Römheld V. (1991) The role of phytosiderophores in acquisition of iron and other micronutrients in graminaceaous species: an ecological approach. *Plant & Soil* **130**, 127-134.

Rout G.R. and Das P. (2003) Effect of metal toxicity on plant growth and metabolism: I. Zinc. *Agronomie* **23**, 3-11.

Saratovsky I., Wightman P.G., Pasten P.A., Gaillard J.F., and Poeppelmeier K.R. (2006) Manganese oxides: Parallels between abiotic and biotic structures. *J. Am. Chem. Soc.* **128**, 11188-11198.

Sarret G., Manceau A., Cuny D., VanHaluwyn C., Deruelle S., Hazemann J.L., Soldo Y., EybertBerard L., and Menthonnex J.J. (1998a) Mechanisms of lichen resistance to metallic pollution. *Environ. Sci. Technol.* **32**, 3325-3330.

Sarret G., Manceau A., Spadini L., Roux J.C., Hazemann J.L., Soldo Y., EybertBerard L., and Menthonnex J.J. (1998b) Structural determination of Zn and Pb binding sites in *Penicillium chrysogenum* cell walls by EXAFS spectroscopy. *Environ. Sci. Technol.* **32**, 1648-1655.

Sarret G., Saumitou Laprade P., Bert V., Proux O., Hazemann J.L., Traverse A.S., Marcus M.A., and Manceau A. (2002) Forms of zinc accumulated in the hyperaccumulator *Arabidopsis halleri*. *Plant Physiol.* **130**, 1815-1826.

Schulze D.G., McCaybuis T., Sutton S.R., and Huber D.M. (1995) Manganese Oxidation-States in *Gaeumannomyces*-Infested Wheat Rhizospheres Probed by Micro-Xanes Spectroscopy. *Phytopathology* **85**, 990-994.

Silvester E.J., Manceau A., and Drits V.A. (1997) The structure of monoclinic Na-rich birnessite and hexagonal birnessite. Part 2. Results from Chemical Studies and EXAFS Spectroscopy. *Amer. Mineral.* **82**, 962-978.

Simon L. (2005) Stabilization of metals in acidic mine spoil with amendments and red fescue (*Festuca rubra* L.) growth. *Environ. Geochem. Health* **27**, 289-300.

Smith R.A.H. and Bradshaw A.D. (1992) Stabilization of toxic mine wastes by the use of tolerant plant populations. *Trans. Inst. Min. Metall.* **81**, A230-A237.

St-Cyr L. and Campbell P. (1996) Metals (Fe, Mn, Zn) in root plaque of submerged aquatic plant collected in situ: relations with metal concentrations in adjacent sediments and in the root tissue. *Biogeochemistry* **33**, 45-76.

Tani Y., Miyata N., Iwahori K., Soma M., Tokuda S., Seyama H., and Theng B.K.G. (2003) Biogeochemistry of manganese oxide coatings on pebble surfaces in the Kikukawa River System, Shizuoka, Japan. *Appl. Geochem.* **18**, 1541-1554.

Tani Y., Miyata N., Ohashi M., Ohnuki T., Seyama H., Iwahori K., and Soma M. (2004) Interaction of inorganic arsenic with biogenic manganese oxide produced by a Mn-oxidizing fungus, strain KR21-2. *Environ. Sci. Technol.* **38**, 6618-6624.

Tebo B.M., vanWaasbergen L.G., Francis C.A., He L.M., Edwards D.B., and Casciotti K. (1998) Manganese oxidation by spores of the marine *Bacillus sp*. strain SG-1 - Application for the bioremediation of metal pollution. *New Developments In Marine Biotechnology*, 177-180.

Tebo B.M., Bargar J.R., Clement B.G., Dick G.J., Murray K.J., Parker D., Verity R., and Webb S.M. (2004) Biogenic manganese oxides: Properties and mechanisms of formation. *Annu. Rev. Earth Planet. Sci.* **32**, 287-328.

Teo B.K. (1986) *EXAFS: basic principles and data analysis*. Springer-Verlag.

Thompson I.A., Huber D.M., Guest C.A., and Schulze D.G. (2005) Fungal manganese oxidation in a reduced soil. *Environ. Microbiol.* **7**, 1480-1487.

Thompson I.A., Huber D.M., and Schulze D.G. (2006) Evidence of a multicopper oxidase in Mn oxidation by *Gaeumannomyces graminis* var. *tritici*. *Phytopathology* **96**, 130-136.

Toner B., Fakra S., Villalobos M., Warwick T., and Sposito G. (2005a) Spatially resolved characterization of biogenic manganese oxide production within a bacterial biofilm. *Appl. Environ. Microbiol.* **71**, 1300-1310.

Toner B., Manceau A., Marcus M.A., Millet D.B., and Sposito G. (2005b) Zinc sorption by a bacterial biofilm. *Environ. Sci. Technol.* **39**, 8288-8294.

Toner B., Manceau A., Webb S.M., and Sposito G. (2006) Zinc sorption to biogenic hexagonal-birnessite particles within a hydrated bacterial biofilm. *Geochim. Cosmochim. Acta* **70**, 27-43.

Vangronsveld J., Van Assche F., and Clijsters H. (1995) Reclamation of a bare industrial area contaminated by non-ferrous metals: *In situ* metal immobilization and revegetation. *Environ. Pollut.* **87**, 51-59.

Villalobos M., Toner B., Bargar J., and Sposito G. (2003) Characterization of the manganese oxide produced by *Pseudomonas putida* strain MnB1. *Geochim. Cosmochim. Acta* **67**, 2649-2662.

Villalobos M., Bargar J.R., and Sposito G. (2005) Mechanisms of Pb(II) sorption on a biogenic manganese oxide. *Environ. Sci. Technol.* **39**, 569-576.

Villalobos M., Lanson B., Manceau A., Toner B., and Sposito G. (2006) Structural model for the biogenic Mn oxide produced by *Pseudomonas putida*. *Amer. Mineral.* **91**, 489-502.

Wadsley A.D. (1955) The crystal structure of chalcophanite, $ZnMn_3O_7.3H_2O$. *Acta Crystallogr.* **8**, 165-172.

Warren B.E. (1941) X-ray diffraction in random layer lattices. *Phys. Rev.* **59**, 693-698.

Webb S.M., Tebo B.M., and Bargar J.R. (2005a) Structural characterization of biogenic Mn oxides produced in seawater by the marine *Bacillus sp*. strain SG-1. *Amer. Mineral.* **90**, 1342-1357.

Webb S.M., Tebo B.M., and Bargar J.R. (2005b) Structural influences of sodium and calcium ions on the biogenic manganese oxides produced by the marine *Bacillus sp*., strain SG-1. *Geomicrobiol. J.* **22**, 181-193.

FIGURE CAPTIONS

Fig. 1. Roots of *Festuca rubra* grown on a Zn-contaminated sediment. Optical microphotograph (**a**), and scanning electron microscope image with (**b**) backscattered electrons and (**c**) secondary electrons.

Fig. 2. Tricolor (RGB) μ-XRF map of a root with Mn-Zn precipitates. Red codes for Ca, green for Zn, and blue for Mn. Each pixel is colored in proportion to Ca-, Zn- and Mn-Kα signals. Pixel size is 7×7 μm^2. The graph is a pixel-by-pixel scatterplot of Zn counts vs. Mn counts, showing the constant Zn:Mn ratio.

Fig. 3. Manganese K-edge EXAFS spectra of Mn-Zn precipitate (dotted lines) and the following references (solid lines): hollandite (Hol), todorokite (Todo), triclinic birnessite (TcBi), lithiophorite (Lit), low-pH hexagonal birnessite (HBi), chalcophanite (Chalco), and δ-MnO_2 (dBi, synthetic turbostratic birnessite).

Fig. 4. Fourier transforms (FTs) of the *k*-weighted Mn-EXAFS spectra for the Mn-Zn precipitate (dotted lines) and synthetic ^{VI}Zn-sorbed δ-MnO_2 (dBi), chalcophanite (Chalco), hexagonal birnessite (HBi), and lithiophorite (Lit). E and TC subscripts denote Mn-Mn contributions from octahedral linked by edges and triple-corners, respectively.

Fig. 5. Zinc K-edge EXAFS spectra. (**a-c**) Overlay plots of the Mn-Zn precipitate spectrum (dotted line) with natural ^{IV}Zn-containing turbostratic birnessite (vernadite, sample 6KR) from Manceau et al. (2007b; **a**, solid line – Sum-sq = 0.12), $^{VI/IV}$Zn-sorbed δ-MnO_2 (dBi) from Toner et al. (2006; **b**, solid line – Sum-sq = 0.83), and a least-squares fit of the Mn-Zn precipitate spectrum to a linear combination of the model compounds in (**a**) and (**b**) (**c**, solid line – Sum-sq = 0.06). The arrows in (**a**) point out the phase misfit when the ^{VI}TC Zn species is omitted in the simulation. The dBi

sample contains 42 (±5) mol% ^{IV}TC Zn and 58 (±5) mol% ^{VI}TC Zn (Toner et al., 2006). Substituting chalcophanite for dBi in the two-component fit yielded the same fraction of TC species and a similar Sum-sq residual (0.07). (**d**) Overlay plot of the Mn-Zn precipitate spectrum (dotted line) and of the Root spectrum (solid line – Sum-sq = 0.10). (**e-g**) Overlay plots of the Root spectrum (dotted line) with organic model compounds (solid line): Zn sorbed on a biofilm at 5.6 10^{-4} mol of Zn per gram of biosorbent from Toner et al. (2005b; **e**, Zncell7 – Sum-sq = 0.052), Zn citrate from Sarret et al. (2002; **f**, – Sum-sq = 0.089), Zn phytate from Sarret et al. (2002; **g**, – Sum-sq = 0.089), Zn sorbed on *Penicillium chrysogenum* at 1.5 10^{-4} mol of Zn per gram of biosorbent from Sarret et al. (1998b; **h**, – Sum-sq = 0.13). The Sum-sq values are calculated as the squares of the residuals, normalized to the sum of the squares of the data values over the [3.0 - 10.5 $Å^{-1}$] *k* interval.

Fig. 6. XRD pattern of Mn-Zn precipitate after subtraction of the scattering from the root.

Fig. 7. Simulations of the [20,11] and [02,31] X-ray scattering bands (C-centered layer cell). Black crosses are experimental data, and red lines are calculated profiles. Small but significant misfits between experimental and calculated patterns are pointed out with arrows. Diffracted intensities were calculated with a turbostratic layer stacking (no interlayer correlation). (**a**) Initial model with 0.186 vacant layer sites and no interlayer Mn. (**b**) Optimal model (Table 1; Figs. 8 and EA-5). (**c**) Model with *a* = 5.014 Å and *b* = 2.895 Å (hexagonal layer symmetry). (**d**) Model with *a* = 5.100 Å and *b* = 2.850 Å (orthogonal layer symmetry). (**e**) Model with all interlayer Mn cations (0.056 per octahedron) located in ^{VI}TC sites, instead of 0.046 and 0.010 in ^{VI}TE and ^{VI}TC sites, respectively, in the optimal fit. (**f**) Model with 0.240 Ca per layer octahedron instead of 0.318 in the optimal model. (**g**) Model with 0.150 vacant sites and 0.244 interlayer Zn^{2+} (Zn:Mn = 0.27), compared to 0.220 and 0.388

(Zn:Mn = 0.46) in the optimal fit. (**h**) Model with 50% tetrahedral and 50% octahedral Zn^{2+}, instead of 77% and 23% in the optimal fit. Unless specified, all parameters used in calculations are those of the optimal model.

Fig. 8. Idealized structure for the Mn-Zn root precipitate with structural formula $[(Mn_{0.78}Vac_{0.22})O_2]Mn^{VITC}_{0.010}Mn^{VITE}_{0.046}Zn^{VITC}_{0.088}Zn^{IVTC}_{0.300}Ca_{0.318}(H_2O)_{0.972}]$. The layer charge deficit due to vacant layer sites is balanced by interlayer Zn and Mn above and/or below layer vacancies, and by Ca in the interlayer mid-plane (see Fig. EA-5 for details).

Fig. 9. Calculation of the 001 and 002 reflections for crystallites composed of one (dashed line), two (dotted-dashed line) and three (dot-dot-dashed line) parallel layers randomly stacked perpendicular to the *ab* plane, and optimal fit (red line) to the data (crosses) obtained with an assemblage of diffracting particles containing 1, 2, and 3 layers in the ratio of 2.0:0.3:0.1. Atomic coordinates of the optimal structure model, derived from the simulation of the [20,11] and [02,31] reflections, were used in all calculations (Figs. 7b and 8, Table 1).

Table 1. Structural parameters of Mn-Zn precipitate derived from the simulation of XRD data.

Atom	*x*	*y*	*ζ*	Occ.	*x*	*y*	*ζ*	Occ.
Mn_{layer} (Mn1)	0	0	0	0.780	-	-	-	-
O_{layer} (O1)	0.333	0	1.00	1.00	-0.333	0	-1.00	1.00
$^{TC}Mn_{inter}$ (Mn2)	0	0	2.20	0.005	0	0	-2.20	0.005
$H_2O_{inter.}$ (O2)	-0.333	0	3.45	0.015	0.333	0	-3.45	0.015
$^{TE}Mn_{inter}$ (Mn3)	-0.333	0	2.20	0.023	0.333	0	-2.20	0.023
$H_2O_{inter.}$ (O3)	0	0	3.45	0.069	0	0	-3.45	0.069
$^{VI}Zn_{inter}$ (Zn1)	0	0	2.20	0.044	0	0	-2.20	0.044
$H_2O_{inter.}$ (O2)	-0.333	0	3.45	0.132	0.333	0	-3.45	0.132
$^{IV}Zn_{inter}$ (Zn2)	0	0	1.77	0.150	0	0	-1.77	0.150
$H_2O_{inter.}$ (O4)	0	0	3.70	0.150	0	0	-3.70	0.150
Ca_{inter} (Ca1)	-0.410	0	3.60	0.053	0.410	0	-3.60	0.053
Ca_{inter} (Ca1)	-0.295	0.115	3.60	0.053	0.295	0.115	-3.60	0.053
Ca_{inter} (Ca1)	-0.295	-0.115	3.60	0.053	0.295	-0.115	-3.60	0.053
$H_2O_{inter.}$ (O5)	0.220	0	3.60	0.04	-0.220	0	-3.60	0.04
$H_2O_{inter.}$ (O5)	-0.110	0.330	3.60	0.04	-0.110	-0.330	-3.60	0.04
$H_2O_{inter.}$ (O5)	-0.110	-0.330	3.60	0.04	0.110	-0.330	-3.60	0.04

Note: b = 2.850 Å, $a = b\sqrt{3}$ = 4.936 Å, γ = 90°, and $d_{(001)}$ = 7.20 Å. *x* and *y* coordinates are expressed as fractions of the *a* and *b* parameters, respectively. Coordinates along the *c**

axis, ζ, are expressed in Å to point out the thickness of layer and interlayer polyhedra. The average dimension of the coherent scattering domains (CSDs) along the *c** axis is 1.2 layers (8.6 Å). The average radius of the disk-like CSDs in the *ab* plane is 33 Å. This value was calculated by fitting the [20,11] reflection. Un-refined thermal B factors are 0.5 $Å^2$ for Mn_{layer}, 1.0 $Å^2$ for O_{layer}, interlayer Mn, and interlayer Zn, and 2.0 $Å^2$ for Ca^{2+} and H_2O.

Table 2. Selected interatomic distances for the optimal structure model.

Atomic pair	Distance (Å)	Atomic pair	Distance (Å)
Mn_{layer}-O_{layer}	1.925		
$^{TC,TE}Mn_{inter.}$-O_{layer}	2.04	$^{TC,TE}Mn_{inter.}$-H_2O	2.07
$^{VI}Zn_{inter.}$-O_{layer}	2.04	$^{VI}Zn_{inter.}$-H_2O	2.07
$^{IV}Zn_{inter.}$-O_{layer}	1.82[a]	$^{IV}Zn_{inter.}$-H_2O	1.93
$Ca_{inter.}$-O_{layer}	2.89	H_2O_{inter}-O_{layer}	2.66
Mn_{layer}-$^{VI}Zn_{inter}$	3.60	Mn_{layer}-$^{IV}Zn_{inter}$	3.35
Mn_{layer}-$^{TC}Mn_{inter.}$	3.60	Mn_{layer}-$^{TE}Mn_{inter.}$	2.75[b]

(a) The $^{IV}Zn_{inter.}$-O_{layer} distance should be increased by ~0.1 Å to provide more realistic Zn-O bond valence (Table EA-1). This cannot be achieved by changing the *z* coordinate of ^{IV}Zn (Fig. EA-6b). Alternatively, moving apart the three oxygen atoms delimiting the underlying vacancy by 0.15 Å in the [110], $[\bar{1}00]$, and $[0\bar{1}0]$ directions increases the $^{IV}Zn_{inter.}$-O_{layer} distance from 1.82 Å to 1.95 Å, as discussed in Manceau et al. (2002a).

[b] The Mn_{layer}-$^{TE}Mn_{inter.}$ distance can be increased by ~0.1 Å by shifting Mn_{inter} in the *ab* plane from its ideal TE position towards the nearest vacant site (see Fig. EA-5). This shift occurs along the $a \pm 120°$ directions with equal probabilities resulting in an increased Debye-Waller B factor without significant alteration of the fit quality.

Table EA-1. Empirical bond-valences for Mn-Zn precipitate[a].

	O1[b]	O1[c]	O1[d]	O1[e]	O2, O3	O3	O4	Σ	Formal valence
Mn1	0.628 ×6→ ×3↓	0.628 ×2↓	0.628 ×2↓	0.628 ×2↓				3.8	4
Mn2, Mn3		0.469 ×3→			0.433 ×3→			2.7	3
Zn1			0.403 ×3→			0.372 ×3→		2.3	2
Zn2				0.731 ×3→			0.543	2.7	2
H^+	0.11[f]								
Σ	1.9 – 2.0[g]	1.7	1.7	2.0					

(a) Bond valences in valence unit (v.u.) were calculated using the Valence for Dos program (v. 2.0 - http://www.ccp14.ac.uk/solution/bond_valence/index.html) and the parameters from Brese and O' Keeffe (1991).

(b) O1 coordinated to 3 Mn^{4+} in Mn1 (Table 1).

(c) O1 coordinated to 2 Mn^{4+} in Mn1 and 1 Mn^{3+} in Mn2 or Mn3.

(d) O1 coordinated to 2 Mn^{4+} in Mn1 and 1 Zn^{2+} in Zn1.

(e) O1 coordinated to 2 Mn^{4+} in Mn1 and 1 Zn^{2+} in Zn2.

(f) O5-H-O1 H-bond.

(g) Depending on whether this O1 receives additional valence from H^+ through H-bond.

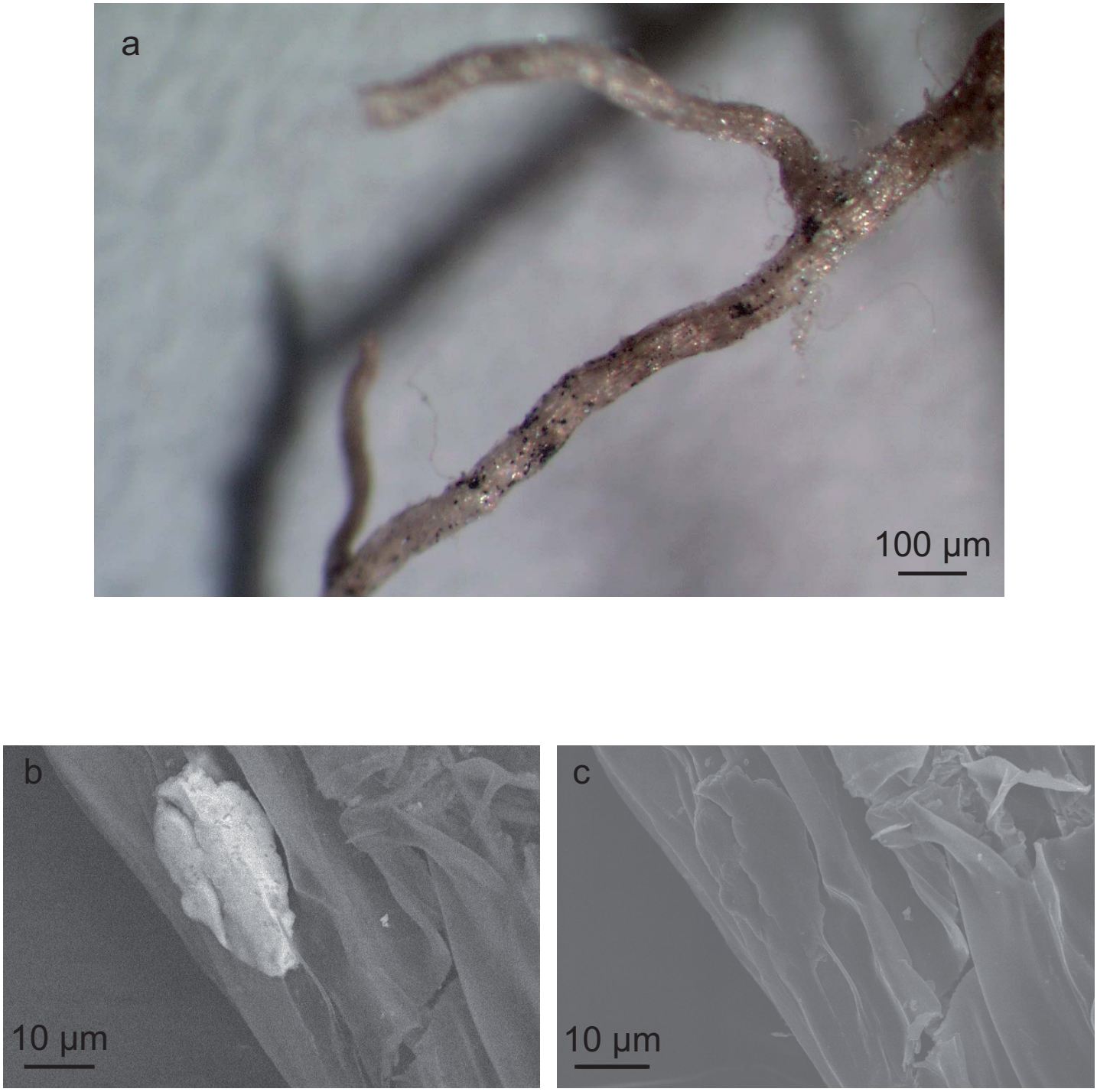

Lanson et al., Fig. 1

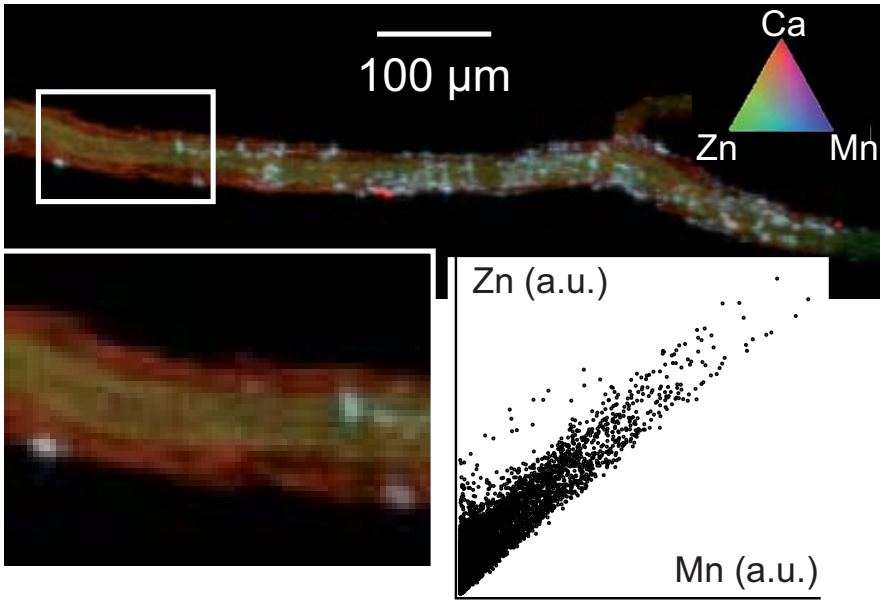

Lanson et al., Fig. 2

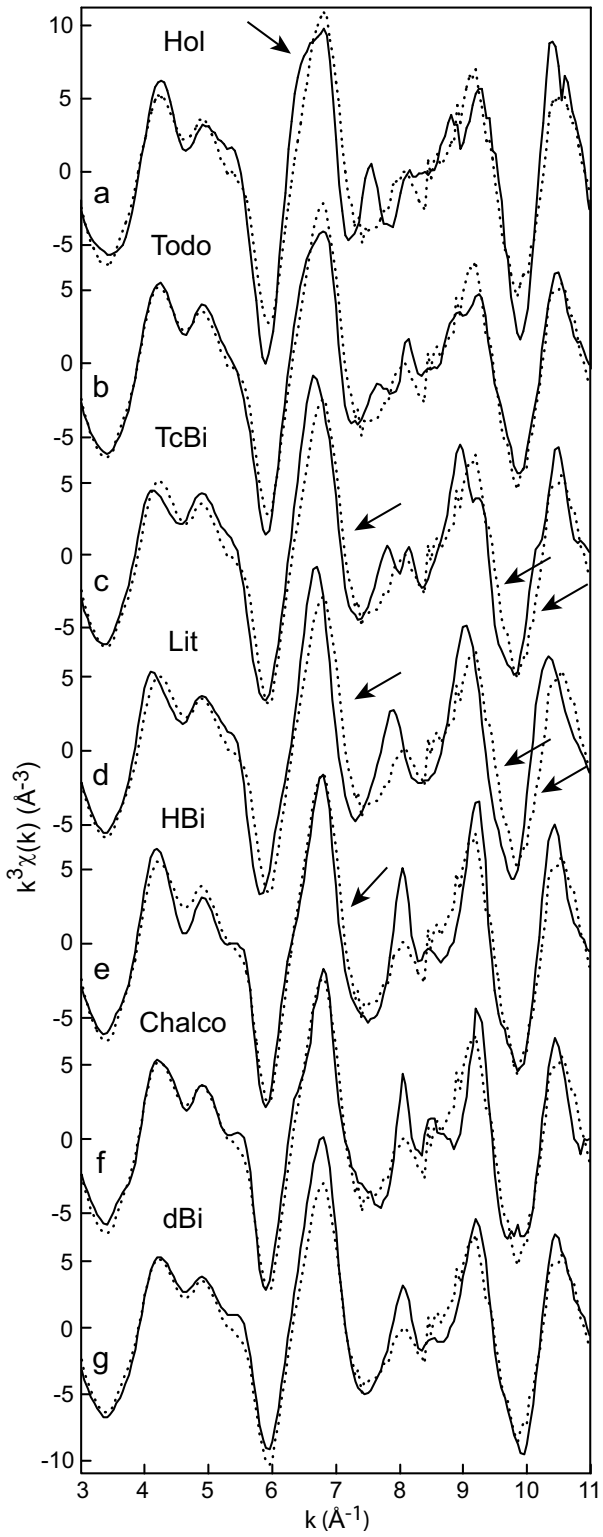

Lanson et al., Fig. 3

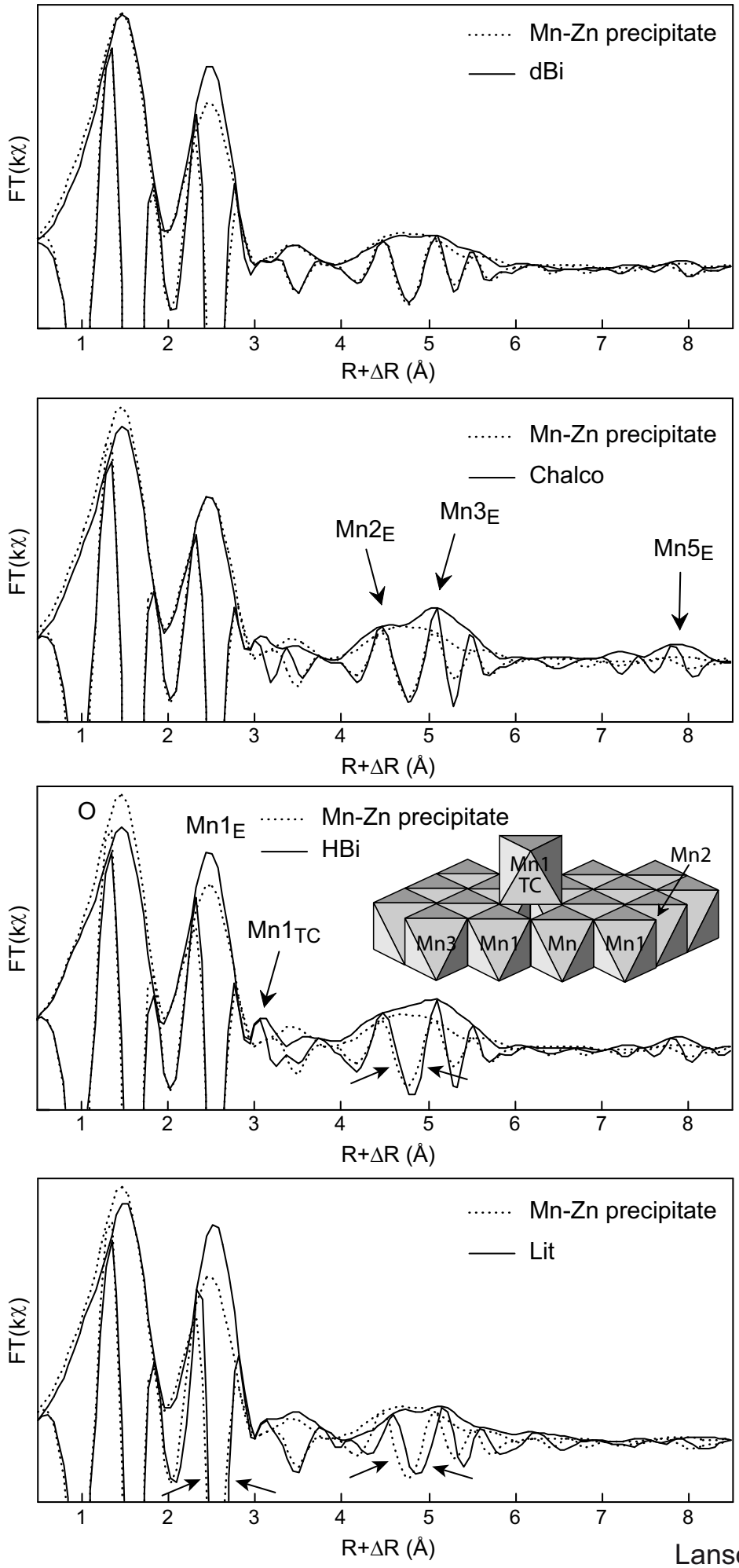

Lanson et al., Fig. 4

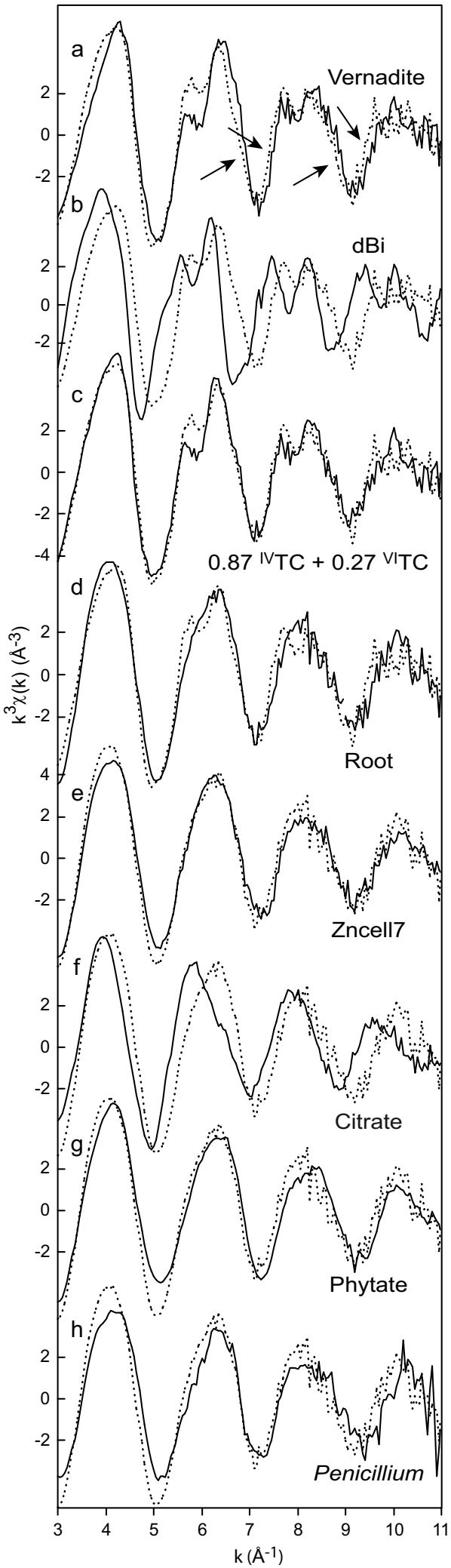

Lanson et al., Fig. 5

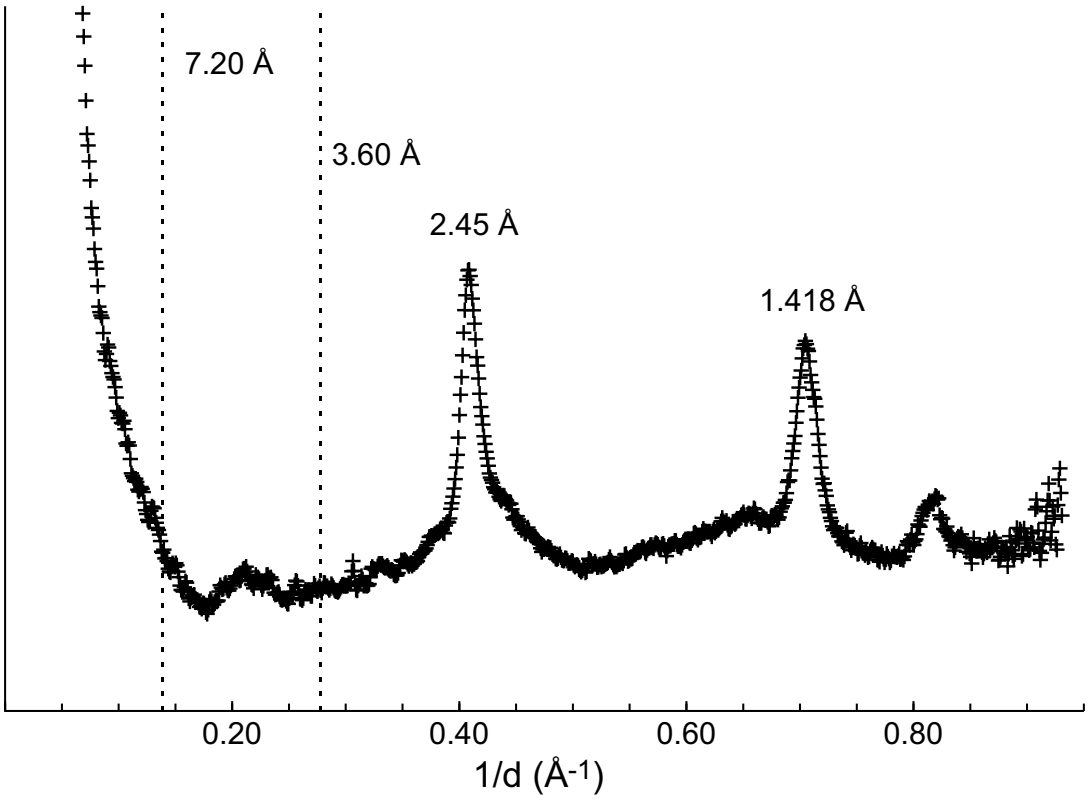

Lanson et al., Fig. 6

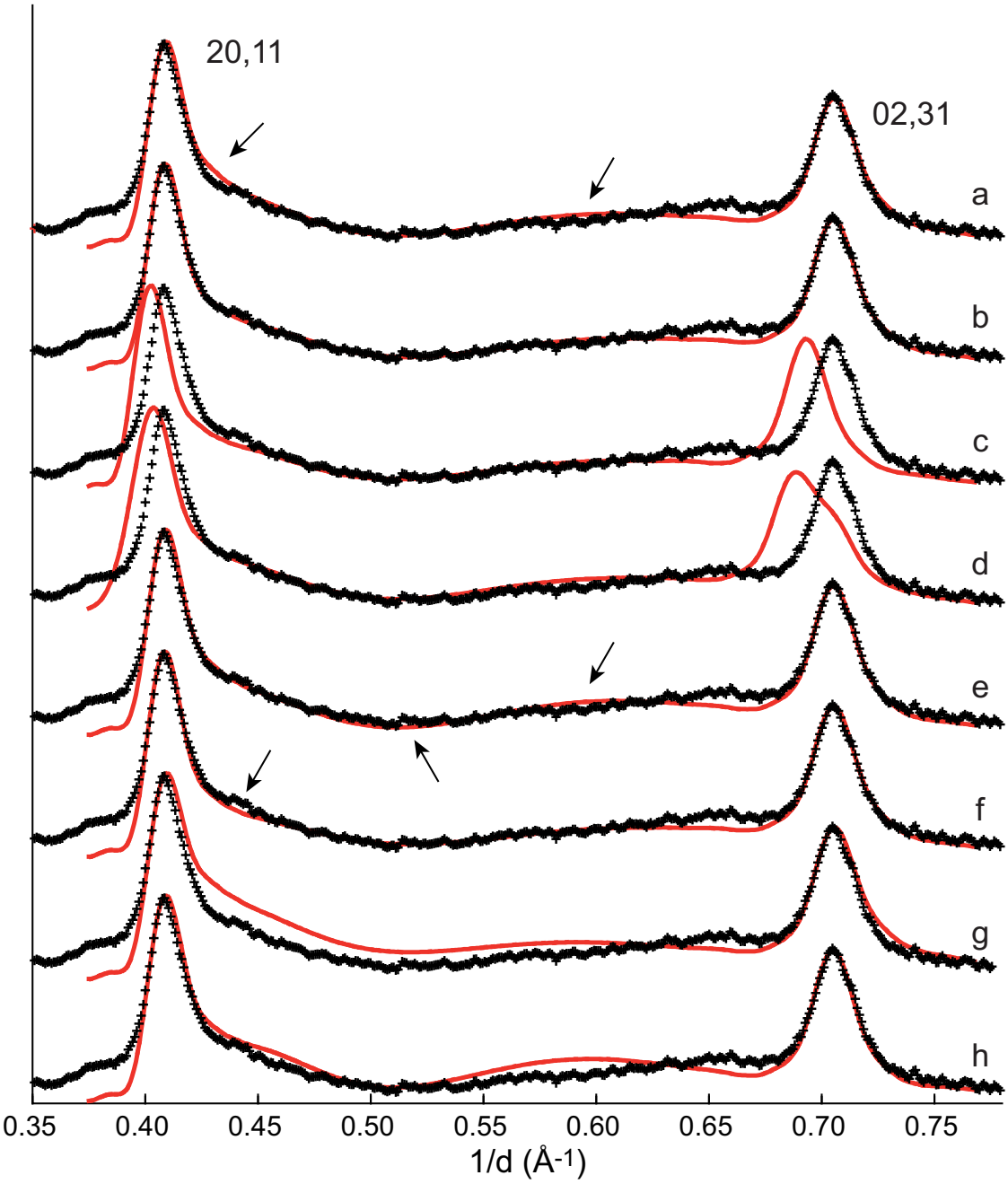

Lanson et al., Fig. 7

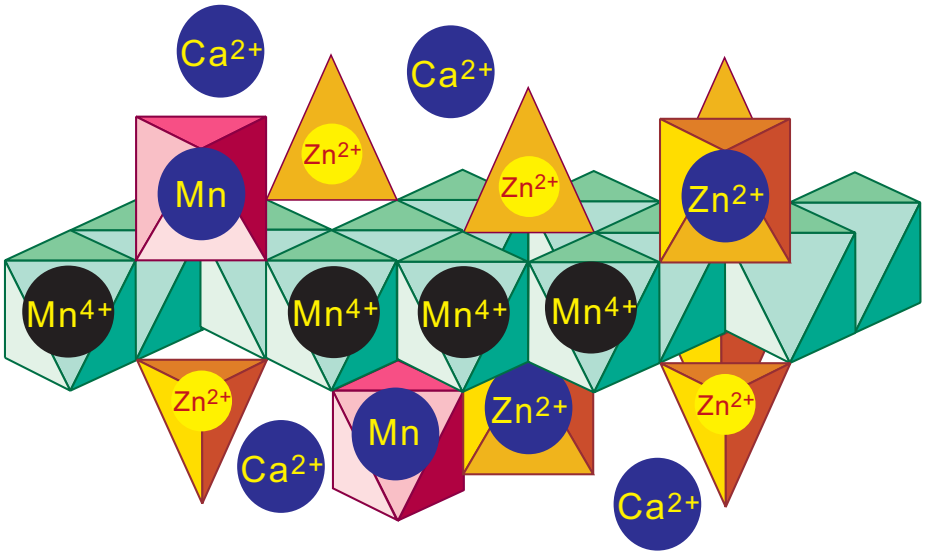

Lanson et al., Fig. 8

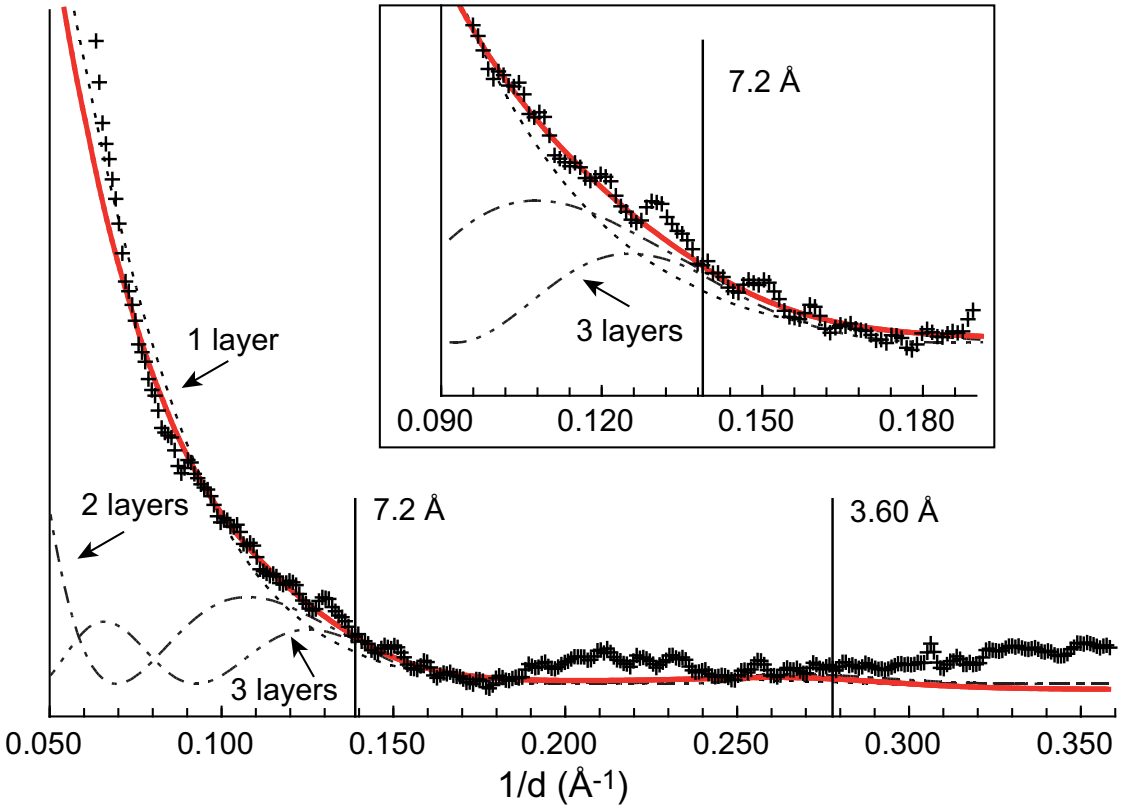

Lanson et al., Fig. 9

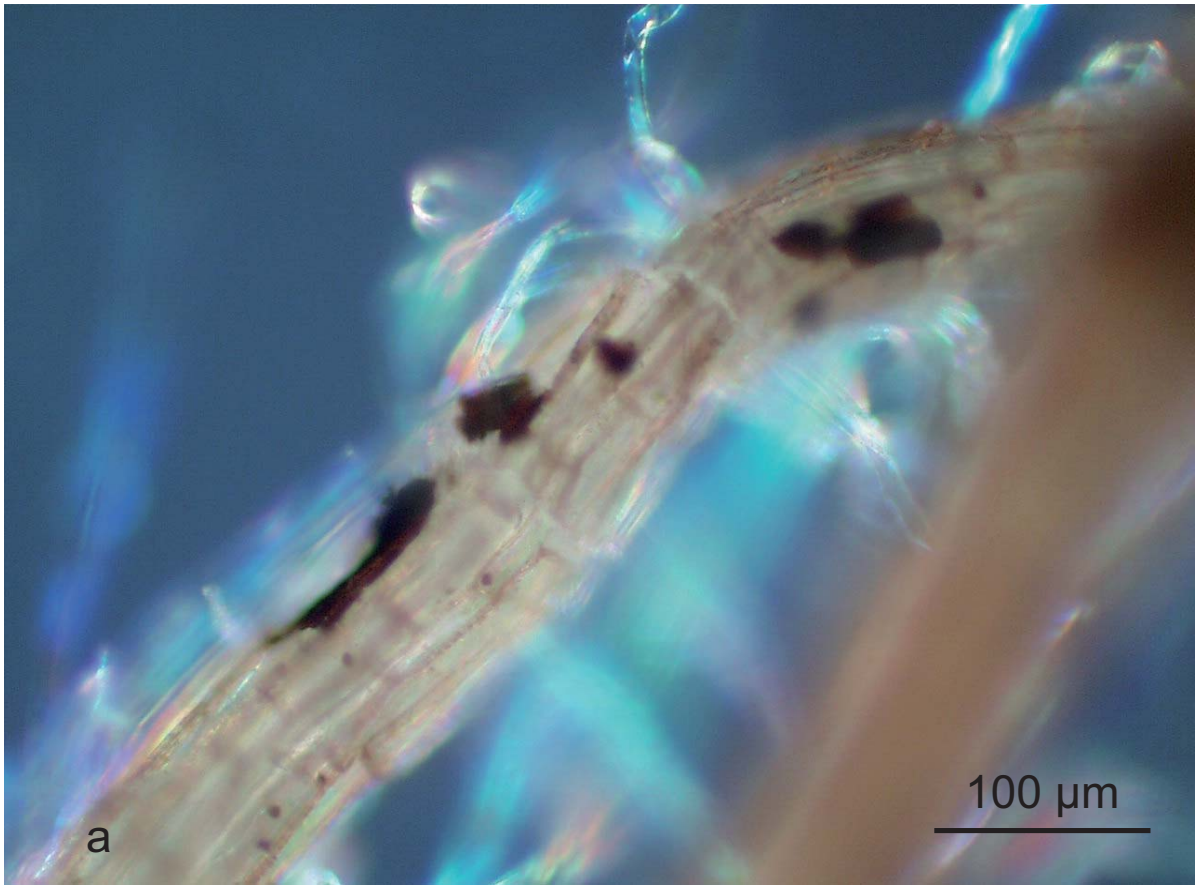

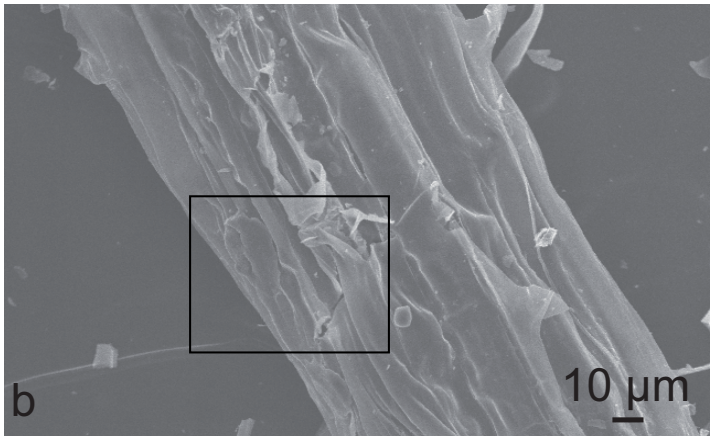

Fig. EA-1: Roots of *Festuca rubra* grown on a Zn-contaminated sediment. (**a**) Close-up photograph from Fig. 1a. (**b**) Lower magnification of Fig. 1c.

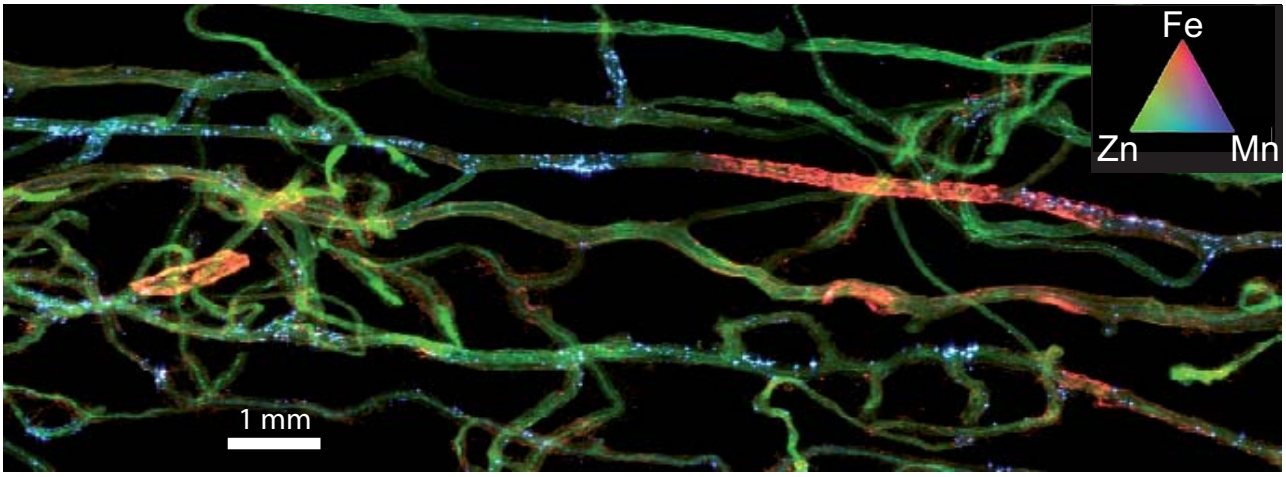

Fig. EA-2: Tricolor (RGB) μ-XRF map of a bundle of roots. Red codes for Fe, green for Zn, and blue for Mn. Each pixel is colored in proportion to Fe-, Zn- and Mn-Kα signals. Pixel size is 18 × 15 μm^2.

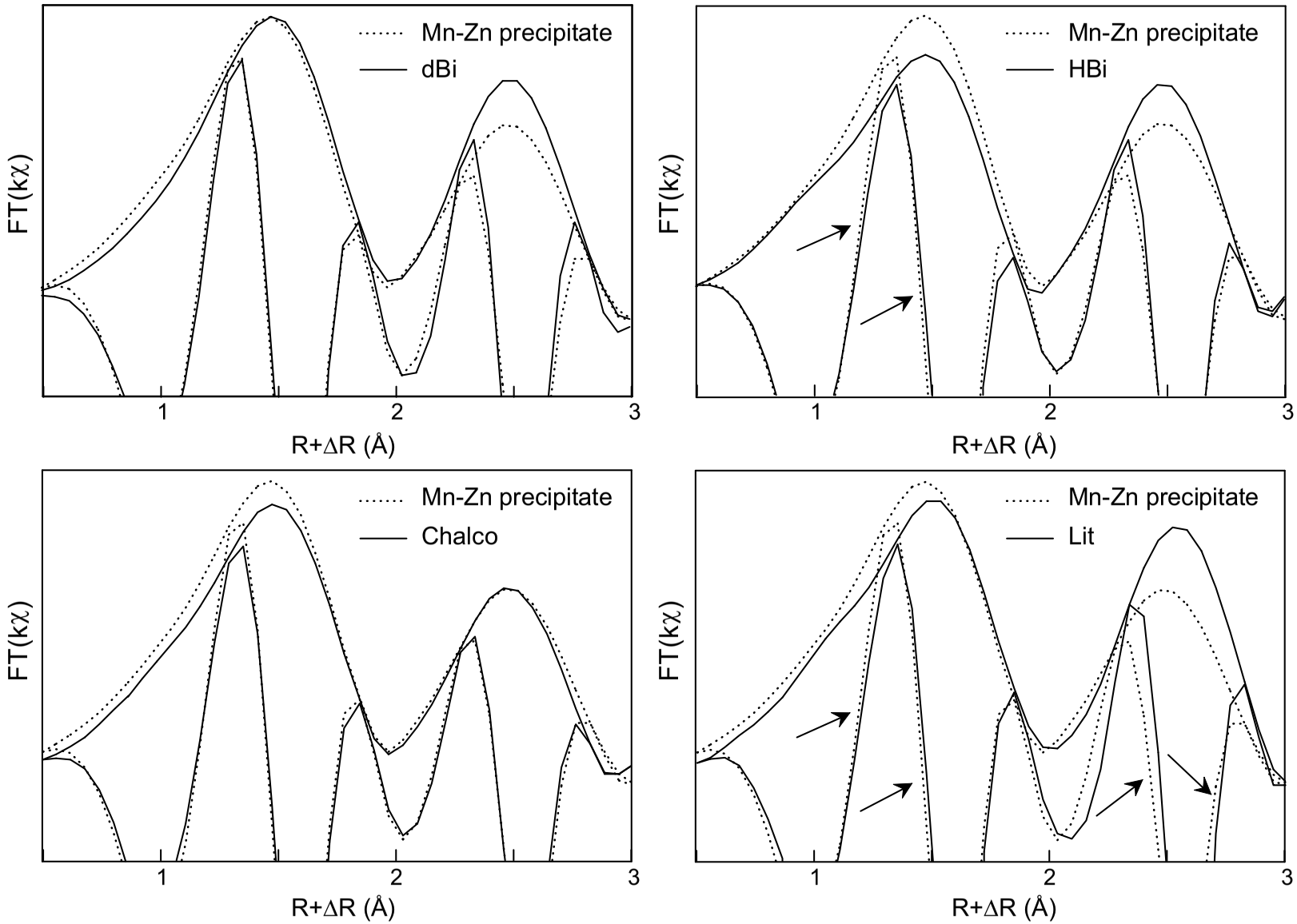

Fig. EA-3: Fourier transforms (FTs) of the manganese K-edge *k*-weighted EXAFS spectra for the Mn-Zn root precipitate and synthetic ^{VI}Zn-sorbed δ-MnO_2 (dBi, synthetic turbostratic birnessite), chalcophanite (Chalco), hexagonal birnessite (HBi), and lithiophorite (Lit). Expansion of the [1-3 Å] R+ΔR interval.

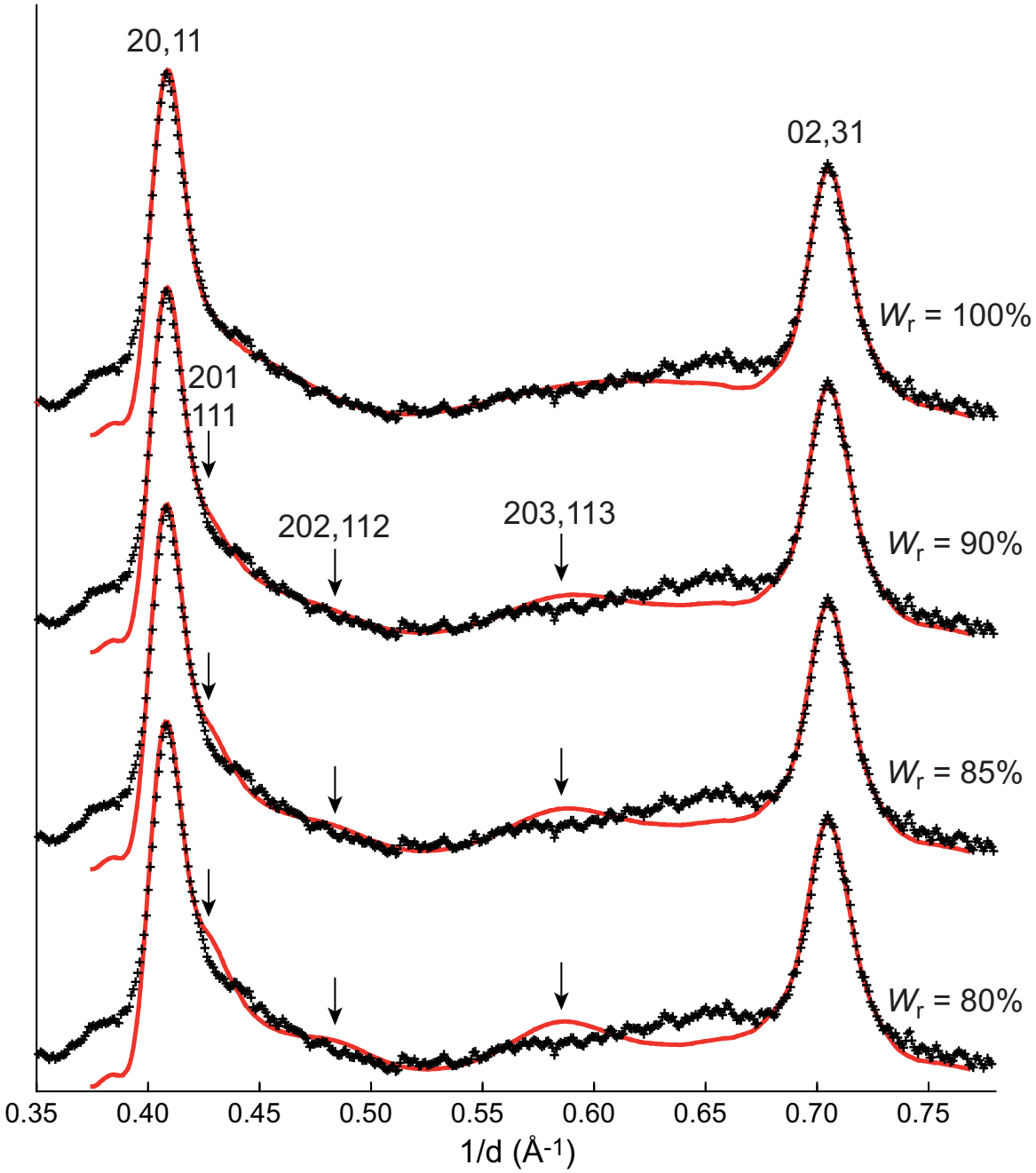

Fig. EA-4: Simulations of the [20,11] and [02,31] X-ray scattering bands (black crosses, C-centered layer cell). Intensities (red lines) were calculated for the optimal structure model (Table 1) with different occurrence probabilities of random stacking faults (W_r). Arrows indicate the positions of *hkl* reflections.

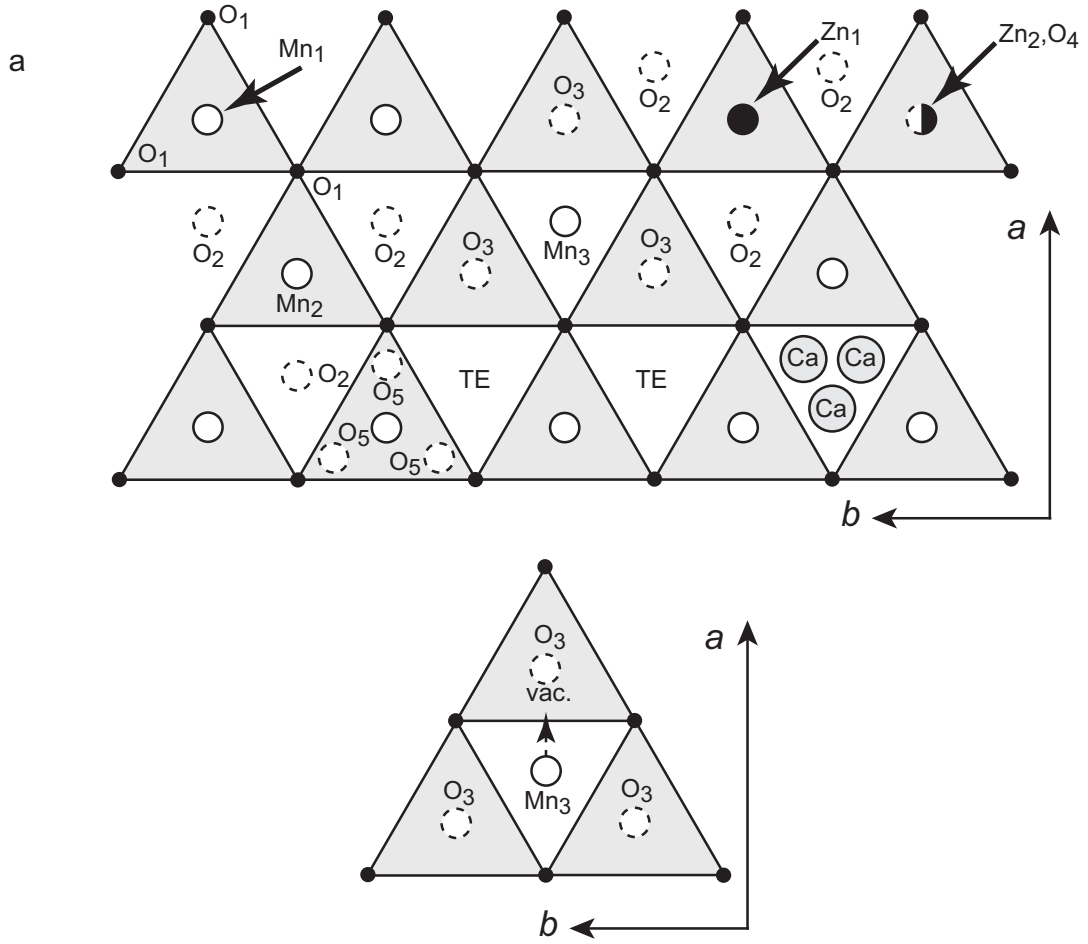

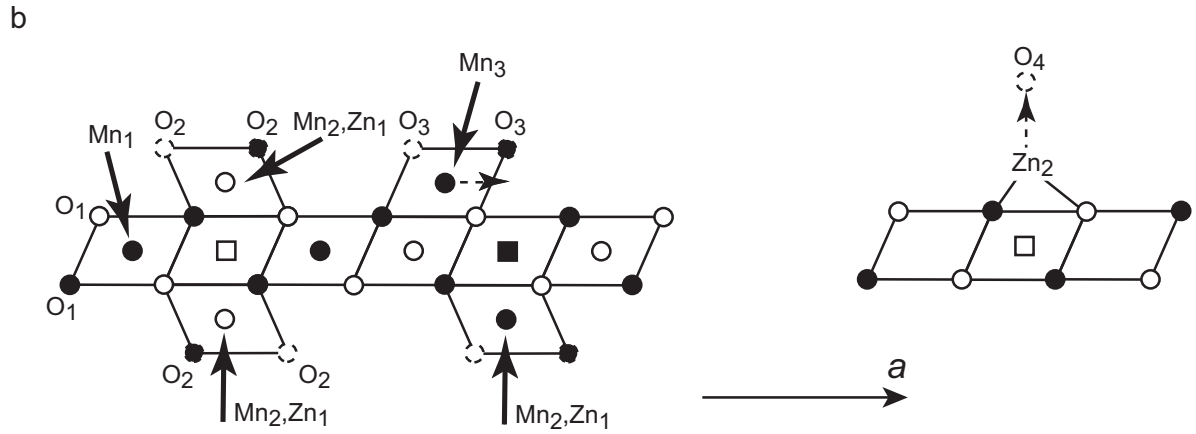

Fig. EA-5: Idealized structure of Mn-Zn precipitate. (**a**) Projection on the *ab* plane. The upper surface of the layer is shown as light shaded triangles, and the atomic notations are the same as in Table 1. (**b**) Projection along the *b* axis. Open and solid symbols indicate atoms at $y = 0$ and $y = \pm½$, respectively. Squares represent vacant layer octahedra.The Mn_3 and Zn_2 atoms can be shifted from their positions as indicated by the dashed arrows to obtain more realistic interatomic distances (see Table EA-1).

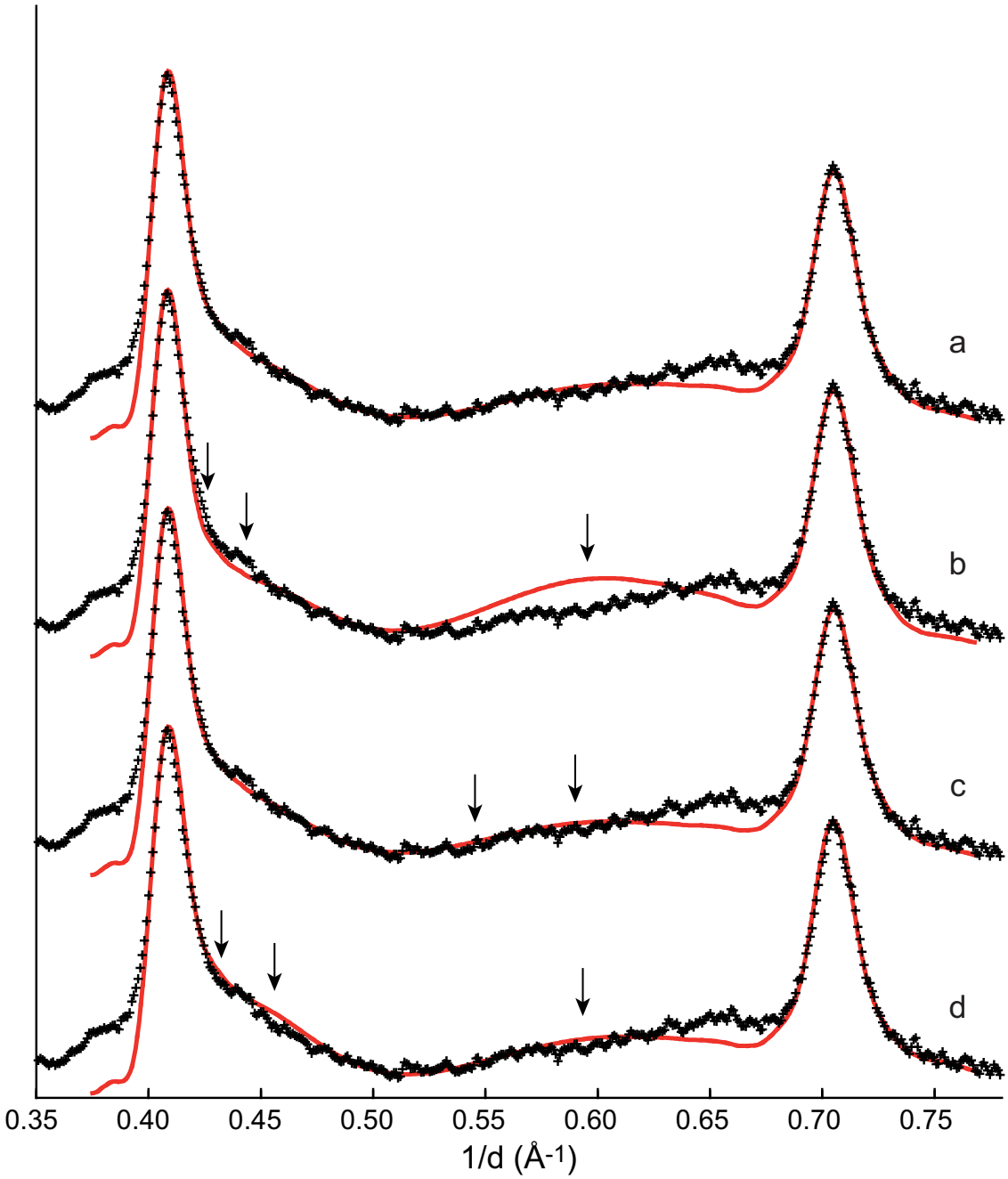

Fig. EA-6: Simulations of the [20,11] and [02,31] X-ray scattering bands (C-centered layer cell, black crosses). Small but significant misfits between experimental and calculated patterns are pointed out with arrows. Intensities (red lines) were calculated with a turbostratic layer stacking (no interlayer correlation). (a) Optimal model (Table 1; Figs. 8 and EA-5); R_{wp} = 3.49%. (b) Model with ^{IV}Zn (Zn2) in (0, 0, 1.97 Å), instead of (0, 0, 1.77 Å) in the optimal fit, so as to increase the Zn-O bond length from 1.82 À (Table 2) to 1.91 Å. Coordinated H_2O molecules (O4) were moved from (0, 0, 3.70 Å) to (0, 0, 3.90 Å); R_{wp} = 3.92%. (c) Model with ^{VI}Zn (Zn1) in (0, 0, 2.30 Å), instead of (0, 0, 2.20 Å) in the optimal fit so as to decrease the sum valence of Zn1 from 2.3 (Table EA-1) to 2.0. Coordinated H_2O molecules (O2) were moved from (-0.333, 0, 3.45 Å) to (-0.333, 0, 3.65 Å); R_{wp} = 3.55%. (d) Model with Ca in (-0.333, 0, 3.60 Å), instead of (-0.410, 0, 3.60 Å) and equivalent positions in the optimal fit; R_{wp} = 3.51%. Unless specified, all parameters used in calculations are those of the optimal model.

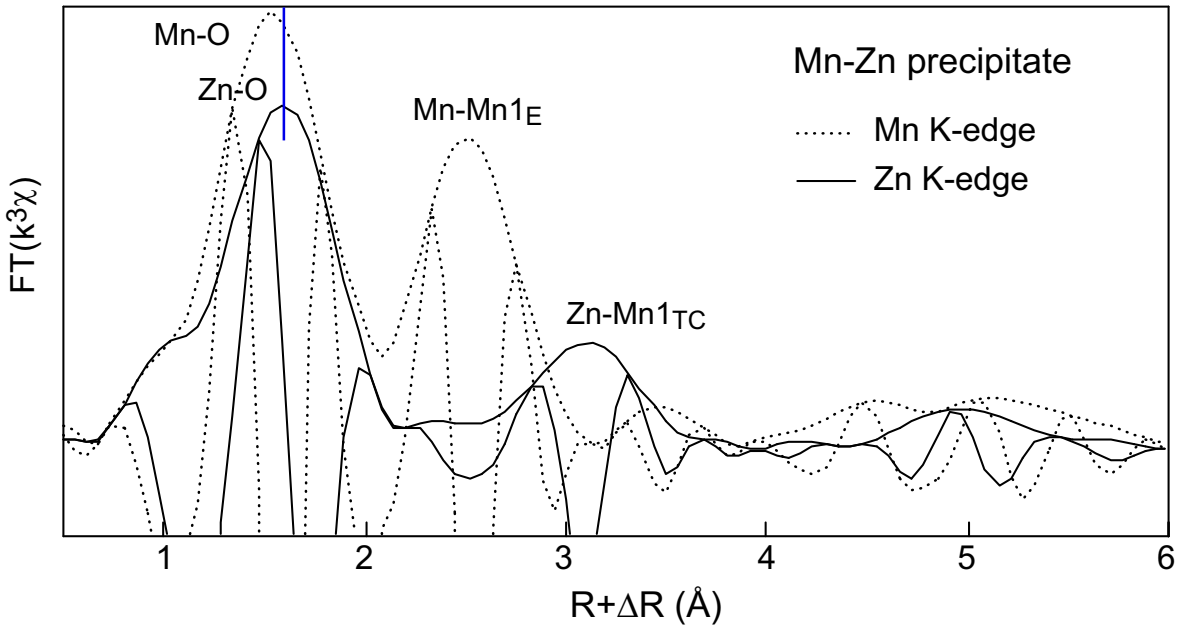

Fig. EA-7: Fourier transform of the EXAFS spectra for the Mn-Zn precipitate at the Mn and Zn K-edges. The average Mn-O and Zn-O EXAFS distances (R values) are 1.90 Å and 2.00 Å, respectively.